

General Relativistic Magnetohydrodynamic Simulations of Jet Formation and Large-Scale Propagation from Black Hole Accretion Systems

Jonathan C. McKinney*

Institute for Theory and Computation, Harvard-Smithsonian Center for Astrophysics, 60 Garden Street, MS 51, Cambridge, MA 02138, USA

Accepted 2006 March 01. Received 2006 February 25; in original form 2006 January 06

ABSTRACT

The formation and large-scale propagation of Poynting-dominated jets produced by accreting, rapidly rotating black hole systems are studied by numerically integrating the general relativistic magnetohydrodynamic equations of motion to follow the self-consistent interaction between accretion disks and black holes. This study extends previous similar work by studying jets till $t \approx 10^4 GM/c^3$ out to $r \approx 10^4 GM/c^2$, by which the jet is super-fast magnetosonic and moves at a lab-frame bulk Lorentz factor of $\Gamma \sim 10$ with a maximum terminal Lorentz factor of $\Gamma_\infty \lesssim 10^3$. The radial structure of the Poynting-dominated jet is piece-wise self-similar, and fits to flow quantities along the field line are provided. Beyond the Alfvén surface at $r \sim 10-100 GM/c^2$, the jet becomes marginally unstable to (at least) current-driven instabilities. Such instabilities drive shocks in the jet that limit the efficiency of magnetic acceleration and collimation. These instabilities also induce jet substructure with $3 \lesssim \Gamma \lesssim 15$. The jet is shown to only marginally satisfy the necessary and sufficient conditions for kink instability, so this may explain how astrophysical jets can extend to large distances without completely disrupting. At large distance, the jet angular structure is Gaussian-like (or uniform within the core with sharp exponential wings) with a half-opening angle of $\approx 5^\circ$ and there is an extended component out to $\approx 27^\circ$. Unlike in some hydrodynamic simulations, the environment is found to play a negligible role in jet structure, acceleration, and collimation as long as the ambient pressure of the surrounding medium is small compared to the magnetic pressure in the jet.

Key words: accretion disks, black hole physics, galaxies: jets, gamma rays: bursts, X-rays : bursts

1 INTRODUCTION

Gamma-ray bursts (GRBs), active galactic nuclei (AGN), and black hole x-ray binary systems exhibit relativistic jets that are believed to be driven by accreting black holes (see, e.g., Rees et al. 1982; Begelman et al. 1984; Woosley 1993). Accreting black holes are the highly efficient engines necessary to account for the observed kinematics and energetics of such relativistic jets. Understanding systems powered by black hole accretion requires a general relativistic magnetohydrodynamics (GRMHD) model of the bulk flow dynamics near the black hole where the relativistic jet is launched. The ideal MHD approximation has been shown to be a reasonably valid model to describe the nonradiative dynami-

cally important black hole accretion physics associated with GRBs, AGN, and black hole x-ray binary systems (see, e.g., Phinney 1983; McKinney 2004). This approximation is the foundation of most studies of jets and winds.

We are concerned with explaining how relativistic jets are formed, accelerate, collimate, and what is the resulting structure at large radii. The primarily difficulty has been to explain how observed jets come to be so well-collimated with opening angles of a few degrees, fast with bulk Lorentz factors of up to $\Gamma \sim 10^3$, and why magnetized jets would not be disrupted by instabilities, such as the kink instability. It has not even been known whether the MHD approximation was sufficient to understand the self-consistent production of jets or their observed fast speeds and small opening angles.

GRMHD numerical models of black hole accretion systems have significantly progressed our understanding of relativistic jets. Such simulations have displayed primarily two

* E-mail: jmckinney@cfa.harvard.edu High Res. Figures: <http://rainman.astro.uiuc.edu/~jon/jetlarge.pdf>

types of “jets,” where one is associated with the disk that is mass-loaded by disk material and the other is associated directly with the black hole (De Villiers, Hawley, & Krolik 2003; McKinney & Gammie 2004; De Villiers et al. 2005a).

GRMHD numerical models of winds from the inner part of the accretion disk have found that the Lorentz factor only reaches $\Gamma < 3$ (De Villiers, Hawley, & Krolik 2003; McKinney & Gammie 2004; De Villiers et al. 2005a). This includes GRMHD numerical models of GRBs that showed a disk wind with a velocity of only $v \sim 0.3c$ (Mizuno et al. 2004). Thus, disk winds may not explain jets with high Lorentz factors unless additional physics, such as possibly efficient neutrino-annihilation for GRBs or shock acceleration of particles in general, is included.

The most astrophysically plausible mechanism to generate highly relativistic jets is via the electromagnetic extraction of black hole spin energy by the Blandford-Znajek (BZ) mechanism (Blandford & Znajek 1977). They modelled the disk as a current sheet that sources the magnetic field that couples to a rotating black hole, which spins down due to a transfer of rotational energy of the space-time to the magnetic field. However, their force-free model does not include matter, and so cannot directly explain the Lorentz factor of observed jets. Also, the BZ model does not self-consistently determine the current in the disk or the field geometry that threads the black hole. All these features require the inclusion of matter, or the inertial effects of matter, that would be present in an accretion disk.

GRMHD numerical models of black hole accretion have shown polar regions with Poynting-dominated jets that are consistent with being powered by the BZ effect (McKinney & Gammie 2004; Komissarov 2005; McKinney 2005a). They have also shown that the magnetic field corresponding to the Blandford-Znajek effect dominates all other magnetic field geometries (Hirose et al. 2004; McKinney 2005a). In contrast to the disk wind that is self-consistently mass-loaded by the disk itself, the Poynting-dominated jet that is launched by the BZ effect has an arbitrary Lorentz factor that is determined by the detailed high-energy physics of the mass-loading of the jet, so low mass-loading can explain highly relativistic jets (see, e.g. Phinney 1983; Beskin 1997; Punsly 2001; Levinson 2005; McKinney 2005a,b).

We study a generic black hole accretion system in the GRMHD approximation and consider its application to all black hole accretion systems. This unification scheme works because the GRMHD equations of motion scale arbitrarily with the mass of the black hole and the mass accretion rate. Hence, a GRMHD model can be applied to any black hole accretion system as a unified model, apart from important high-energy effects that break this scale invariance.

The primary modifications to the GRMHD model come from radiative and other high-energy effects. As in any other study, we assume that the results of a GRMHD model are interesting as long as such physics plays a simple role in the bulk jet dynamics. This role includes setting the mass-loading of the Poynting jet, where in our GRMHD model this is set to some fixed value. Also, the jet speed may be slowly modified, such as by Compton scattering or by synchrotron emission of the internal energy. In this case the radiative effects can be treated as small corrections to the background state set by the GRMHD model.

This paper extends the work of McKinney & Gammie

(2004) by studying the self-consistently generated Poynting-dominated jet as it propagates to large distances. A new version of the GRMHD code called HARM (Gammie et al. 2003a) is used to integrate the equations of motion. Unlike prior work, the jet is shown to reach bulk Lorentz factors of $\Gamma \sim 10$ and maximum terminal Lorentz factors with $\Gamma_\infty \lesssim 10^3$ and collimate to narrow half-opening angles of $\theta_j \sim 5^\circ$. The simulated jet is sufficiently fast and collimated to account for jet observations associated with GRBs, AGN, or x-ray binary systems.

Outline of Paper

In Section 2, we discuss the astrophysical systems to which this study can be applied. We discuss the direct or indirect observations of jet speed, collimation, and structure, which are the principle issues this paper attempts to address.

In Section 3, we summarize the equations solved and the units used in the paper. Examples are given for how to apply our results to any astrophysical system.

In Section 4, we present the setup of the numerical model, such as the initial and boundary conditions. The astrophysical applicability of the model setup to GRBs, AGN, and x-ray binaries is considered.

In Section 5, we present the results of a fiducial numerical model and describe the jet formation, structure, and propagation to large distances. Both the radial and angular structures of the jet are studied and data fits to flow quantities are given. The jet characteristic structure, such as the formation of a double transonic (trans-fast) flow, is discussed.

In Section 6, we discuss the results and their implications. The results are compared to similar investigations, and the limitations of the models presented are discussed.

In Section 7, we provide a short summary of the key points.

2 ASTROPHYSICAL MOTIVATION

Observations associated with GRBs, AGN, and black hole x-ray binary systems all show direct evidence of relativistic outflows. While AGN and x-ray binaries show direct evidence of jet collimation, outflows associated with GRBs are believed to be collimated based on achromatic breaks in afterglow light curves. However, the formation, structure, acceleration, and collimation of relativistic jets are not yet understood. The following discussion outlines the motivation for using a GRMHD model to study jets from GRBs, AGN, and x-ray binary systems.

2.1 GRBs

Neutron stars and black holes are associated with the most violent of post-Big Bang events: supernovae and some GRBs and maybe some x-ray flashes (XRFs) (for a general review see Woosley 1993; Wheeler, Yi, Höflich, & Wang 2000). Observations of a supernova light curve (SN2003dh) in the afterglow of GRB 030329 suggest that at least some long-duration GRBs are consistent with core-collapse events (Stanek et al. 2003; Kawabata et al. 2003; Uemura et al. 2003; Hjorth et al. 2003).

Neutrino processes and magnetic fields are both important to understand core-collapse. In unraveling the mechanism by which core-collapse supernovae explode, the details of the neutrino transport model was at some point realized to be critical to whether a supernova is produced in simulations (Messer et al. and collaborators 1998). This has thus far been interpreted to imply that highly accurate neutrino transport physics is required, but this could also mean additional physics, such as a magnetic field, could play a significant role. Indeed, all core-collapse events may be powered by MHD processes rather than neutrino processes (Leblanc & Wilson 1970; Symbalisty 1984; Woosley & Weaver 1986; Duncan & Thompson 1992; Khokhlov et al. 1999; Akiyama, Wheeler, Meier, & Lichtenstadt 2003). Core-collapse involves shearing subject to the Balbus-Hawley instability as in accretion disks (Akiyama, Wheeler, Meier, & Lichtenstadt 2003), and this process creates a dynamically important magnetic field during collapse. All core-collapse explosions are significantly polarised, asymmetric, and often bi-polar indicating a strong role of rotation and a magnetic field (see, e.g., Wang & Wheeler 1996; Wheeler, Yi, Höflich, & Wang 2000; Wang, Howell, Höflich, & Wheeler 2001; Wang et al. 2002; Wang, Baade, Höflich, & Wheeler 2003, and references therein). Possible evidence for a magnetic dominated outflow has been found in GRB 021206 (Coburn & Boggs 2003), marginally consistent with a magnetic outflow directly from the inner engine (Lyutikov, Pariev, & Blandford 2003), although these observations remain controversial. However, most core-collapse supernovae may still not require magnetic fields (Woosley et al. 2003).

The key energy source for many GRB models is a black hole accretion system since the efficiency is high for converting gravitational binding energy to some type of emission. Collapsar type models are based upon the formation of a black hole during the core-collapse of rapidly rotating massive stars. The typical radius of the accretion disk may determine the duration of long-duration GRBs (Woosley 1993; Paczynski 1998; MacFadyen & Woosley 1999). An accretion disk is also formed as a result of a neutron star or black hole collisions with another stellar object (Narayan et al. 1992, 2001).

GRBs are believed to be the result of an ultrarelativistic jet. Indirect observational evidence of relativistic motion is suggested by afterglow achromatic light breaks and the “compactness problem” suggests GRB material must be ultrarelativistic with Lorentz factor $\Gamma \gtrsim 100$ to emit the observed nonthermal γ -rays (see, e.g., Piran 2005). Direct observational evidence for relativistic motion comes from radio scintillation of the ISM (Goodman 1997) and measurements of the afterglow emitting region from GRB030329 (Taylor et al. 2004a,b).

Typical GRB jet models invoke either a hot neutrino-driven jet or a cold Poynting flux-dominated jet. While both mechanisms extract comparable amounts of the accretion energy to power the jet (Popham et al. 1999), a neutrino-driven jet derives its energy from the annihilation of neutrinos produced by the release of gravitational binding energy, and consequently the jet is thermally accelerated. However, strong outflows can be magneti-

cally driven (Bisnovatyi-Kogan & Ruzmaikin 1976; Lovelace 1976; Blandford 1976; Blandford & Znajek 1977).

2.2 AGN

AGN have long been believed to be powered by accretion onto supermassive black holes (Zel'dovich 1964; Salpeter 1964). Observations of MCG 6-30-15 show an iron line feature consistent with emission from a relativistic disk with $v/c \sim 0.2$ (Tanaka et al. 1995; Fabian et al. 2002), although the lack of a temporal correlation between the continuum emission and iron-line emission may suggest the basic fluorescence model is incorrect. Alternatively, the iron-line may be a jet-related feature (Elvis 2000).

AGN are observed to have jets with $\Gamma \sim 10$ (Urry & Padovani 1995; Biretta et al. 1999), maybe even $\Gamma \sim 30$ (Begeleman et al. 1994; Ghisellini & Celotti 2001; Jorstad et al. 2001), while some observations imply $\Gamma \lesssim 200$ (Ghisellini et al. 1993; Krawczynski et al. 2002; Konopelko et al. 2003). Some radio-quiet AGN show evidence of weak jets (Ghisellini et al. 2004), which could be explained as a disk wind and not require a rapidly rotating black hole (McKinney & Gammie 2004). Observations imply the existence of a two-component jet structure with a Poynting jet core and a dissipative surrounding component (Ghisellini & Madau 1996; Ghisellini et al. 2005). The energy structure of the jet and wind are important in understanding the feedback effect that controls size of the black hole and may determine the $M - \sigma$ relation (Springel et al. 2004; Di Matteo et al. 2005).

2.3 X-ray Binaries

Long after their formation, neutron stars and black holes often continue to produce outflows and jets (Mirabel & Rodríguez 1999). These include x-ray binaries (for a review see Lewin et al. 1995; McClintock & Remillard 2003), neutron star as pulsars (for a review see Lorimer 2001 on ms pulsars and Thorsett & Chakrabarty 1999 on radio pulsars) and soft-gamma ray repeaters (SGRs) (Thompson & Duncan 1995, 1996; Kouveliotou et al. 1999). In the case of x-ray binaries, the companion star's stellar wind or Roche-lobe forms an accretion disk. Many x-ray binaries in their hard/low state (and radio-loud AGN) show a correlation between the x-ray luminosity and radio luminosity (Merloni et al. 2003), which is consistent with radio synchrotron emission from a jet and x-ray emission from a geometrically thick, optically thin, Comptonizing disk.

Some black hole x-ray binaries have jets (Mirabel et al. 1992; Fender 2003a), such as GRS 1915+105 with apparently superluminal motion (Mirabel & Rodriguez 1994; Mirabel & Rodríguez 1999; Fender & Belloni 2004; Kaiser et al. 2004). However, it is difficult to constrain the Lorentz factor, which in some ejection events may be as large for x-ray binaries as for AGN with a Lorentz factor of $\Gamma \lesssim 100$ (Fender 2003b; Miller-Jones et al. 2006). The observed broad, shifted, and asymmetric iron line from GRS 1915+105 is possible evidence for a relativistic accretion disk (Martocchia et al. 2002), although this feature could be produced by a jet component as suggested for AGN.

Gierliński & Done (2004) suggest that at least some systems, such as GRS 1915+105, have slowly rotating black

holes (but see Cui et al. 1998). If this is correct, then the BZ mechanism may not be responsible for these jets. A baryon-loaded disk wind with $\Gamma \lesssim 3$ can be produced from a black hole accretion disk and not require a rapidly rotating black hole (McKinney & Gammie 2004). Nonrelativistic outflows were found even in viscous hydrodynamic simulations (Stone et al. 1999; Igumenshchev & Abramowicz 1999, 2000; McKinney & Gammie 2002).

3 EVOLUTION EQUATIONS AND UNITS

The model is that of a rotating black hole, described by the Kerr metric, surrounded by an accretion disk. The Kerr metric is written in Kerr-Schild coordinates, such that the inner-radial computational boundary can be placed inside the horizon and so out of causal contact with the flow. The Kerr metric in Kerr-Schild coordinates and the Jacobian transformation to Boyer-Lindquist coordinates are given in McKinney & Gammie (2004).

Boyer-Lindquist coordinates are not chosen because it is difficult to avoid interactions between the inner-radial computational boundary and the jet. The coordinate singularity at the event horizon in Boyer-Lindquist can be avoided by placing the inner-radial computational boundary outside the horizon. However, Poynting-dominated flows have waves that propagate outward even arbitrarily close to the event horizon. Using Boyer-Lindquist coordinates can lead to excessive variability in the jet since the ingoing superfast transition is not on the computational grid, and then the details of the boundary condition can significantly influence the jet. Numerical models of viscous flows have historically had related issues (see discussion in, e.g., McKinney & Gammie 2002).

3.1 GRMHD Equations of Motion

The GRMHD notation follows Misner et al. (1973), hereafter MTW. A single-component MHD approximation is assumed such that particle number is conserved,

$$(\rho_0 u^\mu)_{;\mu} = 0, \quad (1)$$

where ρ_0 is the rest-mass density and u^μ is the 4-velocity. A 4-velocity with a spatial drift is introduced that is unique by always being related to a physical observer for any space-time and has well-behaved spatially interpolated values, which is useful for numerical schemes. This 4-velocity is

$$\tilde{u}^i \equiv u^i - \gamma \eta^i, \quad (2)$$

where $\gamma = -u^\alpha \eta_\alpha$. This additional term represents the spatial drift of the zero angular momentum (ZAMO) frame defined to have a 4-velocity of $\eta_\mu = \{-\alpha, 0, 0, 0\}$, where $\alpha \equiv 1/\sqrt{-g^{tt}}$ and so $u^t = \gamma/\alpha$. One can show that $\gamma = (1+q^2)^{1/2}$ with $q^2 \equiv g_{ij} \tilde{u}^i \tilde{u}^j$.

For a magnetized plasma, the conservation of energy-momentum equations are

$$T^{\mu\nu}_{;\nu} = (T_{\text{MA}}^{\mu\nu} + T_{\text{EM}}^{\mu\nu})_{;\nu} = 0, \quad (3)$$

where $T^{\mu\nu}$ is the stress-energy tensor, which can be split into a matter (MA) and electromagnetic (EM) part. In the fluid approximation

$$T_{\text{MA}}^{\mu\nu} = (\rho_0 + u_g) u^\mu u^\nu + p_g P^{\mu\nu}, \quad (4)$$

with a relativistic ideal gas pressure $p_g = (\gamma - 1)u_g$, where u_g is the internal energy density and the projection tensor is $P^{\mu\nu} = g^{\mu\nu} + u^\mu u^\nu$, which projects any 4-vector into the comoving frame (i.e. $P^{\nu\mu} u_\mu = 0$).

In terms of the Faraday (or electromagnetic field) tensor ($F^{\mu\nu}$),

$$T_{\text{EM}}^{\mu\nu} = F^{\mu\gamma} F^\nu{}_\gamma - \frac{1}{4} g^{\mu\nu} F^{\alpha\beta} F_{\alpha\beta}, \quad (5)$$

which is written in Heaviside-Lorentz units such that a factor of 4π is absorbed into the definition of $F^{\mu\nu}$, where the Gaussian unit value of the magnetic field is obtained by multiplying the Heaviside-Lorentz value by $\sqrt{4\pi}$. The induction equation is given by the space components of ${}^*F^{\mu\nu}{}_{;\nu} = 0$, where ${}^*F^{\mu\nu} = \frac{1}{2} \epsilon^{\mu\nu\kappa\lambda} F_{\kappa\lambda}$ is the dual of the Faraday tensor (Maxwell tensor), and the time component gives the no-monopoles constraint. Here ϵ is the Levi-Civita tensor, where $\epsilon^{\mu\nu\lambda\delta} = -\frac{1}{\sqrt{-g}} [\mu\nu\lambda\delta]$ and $[\mu\nu\lambda\delta]$ is the completely antisymmetric symbol. The comoving electric field is defined as

$$e^\mu \equiv u_\nu F^{\mu\nu} = \frac{1}{2} \epsilon^{\mu\nu k\lambda} u_\nu {}^*F_{\lambda k} = \eta j^\nu, \quad (6)$$

where η corresponds to a scalar resistivity for a comoving current density $j^\mu = J_\nu P^{\nu\mu}$. The comoving magnetic field is defined as

$$b^\nu \equiv u_\mu {}^*F^{\mu\nu} = \frac{1}{2} \epsilon^{\mu\nu k\lambda} u_\mu {}^*F_{\lambda k}. \quad (7)$$

The ideal MHD approximation, $\eta = e^\mu = 0$, is assumed, and so the invariant $e^\mu b_\mu = 0$. Since the Lorentz acceleration on a particle is $f_l^\mu = qe^\mu$, then this implies that the Lorentz force vanishes on a particle in the ideal MHD approximation. Since $e^\nu u_\nu = b^\nu u_\nu = 0$, they each have only 3 independent components. One can show that

$${}^*F^{\mu\nu} = b^\mu u^\nu - b^\nu u^\mu, \quad (8)$$

and

$$F^{\mu\nu} = \epsilon^{\mu\nu\sigma\epsilon} u_\sigma b_\epsilon, \quad (9)$$

so that the electromagnetic part of the stress-energy tensor can be written as

$$T_{\text{EM}}^{\mu\nu} = \frac{b^2}{2} (u^\mu u^\nu + P^{\mu\nu}) - b^\mu b^\nu. \quad (10)$$

The other Maxwell equations, $J^\mu = F^{\mu\nu}{}_{;\nu}$, define the current density, J^μ , but are not needed in the ideal MHD approximation for the evolution of the matter or the magnetic field.

For numerical simplicity, another set of field vectors are introduced, such that $B^i \equiv {}^*F^{it}$ and $E_i \equiv F_{it}/\sqrt{-g}$. The two 4-vectors e^μ and b^μ and the 3-vectors B^i and E_i are just different ways of writing the independent components of the Faraday or Maxwell tensors. Equation (7) implies $b^t = B^i u_i$ and $b^i = (B^i + u^i b^t)/u^t$. Then the no-monopoles constraint becomes

$$(\sqrt{-g} B^i)_{,i} = 0, \quad (11)$$

and the magnetic induction equation becomes

$$\begin{aligned} (\sqrt{-g} B^i)_{,t} &= -(\sqrt{-g} (b^i u^j - b^j u^i))_{,j} \\ &= -(\sqrt{-g} (B^i v^j - B^j v^i))_{,j} \\ &= -(\sqrt{-g} (\epsilon^{ijk} \varepsilon_k))_{,j}, \end{aligned} \quad (12)$$

where $v^i = u^i/u^t$, $E_i = \varepsilon_i = -\epsilon_{ijk}v^jB^k = -\mathbf{v} \times \mathbf{B}$ is the electromotive force (EMF), and ϵ^{ijk} is the spatial permutation tensor. The above set of equations are those that are solved. A more complete discussion of the relativistic MHD equations can be found in Anile (1989).

3.2 Floor Model

In GRMHD numerical models of Poynting jets, the black hole's polar region is always completely evacuated (McKinney & Gammie 2004; Komissarov 2004, 2005; De Villiers, Hawley, & Krolik 2003; De Villiers et al. 2005a). Unlike in the radial direction through the disk (Spruit & Taam 1990; Igumenshchev et al. 2003; Narayan et al. 2003), the jet is interchange *stable* across the interface between the disk wind and the Poynting-dominated jet (Levinson & Eichler 1993), so these nonaxisymmetric modes do not lead to significant mass-loading of the Poynting jet. Anomalous resistivity due to reconnection between the wind and funnel is not strong enough to significantly fill the funnel even at modest resolutions that under-resolve the funnel-wall interface (McKinney & Gammie 2004; McKinney 2004). Also, the disk wind, which straddles the Poynting jet, has a sufficiently large angular momentum to avoid significantly contaminating the Poynting jet (see, e.g., Mochkovitch et al. 1993). That is, unlike in the radial direction in the disk, there is no angular momentum transport across the θ direction between the Poynting-dominated and the disk wind. Therefore, to evolve the GRMHD equations of motion, which require matter, a numerical scheme or physical mechanism must be invoked to fill the funnel with matter once it evacuates.

As done by all others, in this paper the rest-mass and internal energy density are limited to a small but finite value in the Poynting-dominated jet by employing a so-called “floor model.” This model forces a minimum on the rest-mass density (ρ_{fl}) and internal energy density (u_{fl}), which are usually set to several orders of magnitude lower than the disk density. This effectively modifies the equations of motion.

Floor-models necessarily violate the ideal MHD approximation because they violate rest-mass and energy-momentum conservation. This occurs, at least, where the poloidal velocity $u^p = 0$ at the stagnation surface in the Poynting-dominated jet. Matter inside the stagnation surface falls into the black hole, while matter outside it is ejected as part of the jet. Arbitrary floor-models violate the ideal-MHD condition far away from the black hole where no rest-mass should be added for any physical mass-loading model (Phinney 1983; McKinney 2004, 2005b). For example, if a numerical model uses $\rho_{fl} \sim \text{Const.}$ and the floor value is reached at small radii, then the ideal-MHD approximation is violated for the entire length of the jet in the funnel because the density would otherwise have decreased with radius.

We use a floor model with a minimum allowed rest-mass density of $\rho_{fl} = 10^{-7}r^{-2.7}\rho_{0,disk}$ and minimum allowed internal energy density of $u_{fl} = 10^{-9}r^{-2.7}\rho_{0,disk}$. The coefficients are not chosen arbitrarily small or large for two reasons. First, the value of b^2/ρ_0 in the jet determines the magnetic energy per unit particle, which determines the maximum Lorentz factor the jet can obtain. As long as $b^2/\rho_0 > 1$ near the poles, then we find that a relativistic jet emerges around the poles. The important physics in the emergence of

a BZ-driven jet is that the gradient in the toroidal magnetic field dominates the gas+ram pressure of the surrounding material. The density floor is chosen to allow the emergence of a fast jet since the magnetic energy per unit particle is large ($b^2/\rho_0 \lesssim 10^7$ since $b^2 \sim \rho_{0,disk}c^2$ is expected near the poles of the black hole) in the jet once it is evacuated. Conversely, if a density floor coefficient is chosen such that $\rho_{fl} \gtrsim 10^{-1}\rho_{0,disk}$, then we find that no Poynting-dominated jet emerges since the value of $b^2/\rho_0 \lesssim 1$ around the black hole near the poles. A self-consistent model of the mass-loading must at least determine the time-averaged density near the black hole around the poles. Second, the floor coefficient is chosen to be not too low in order to avoid numerical difficulties in integrating the equations when the floor is activated in regions of large magnetic energy density per unit rest-mass density. This is a common problem with all present GRMHD numerical methods since the equations of motion become a stiff set of equations in the limit $b^2/\rho_0 \gg 1$.

The radial scaling of the floor model is chosen to avoid contamination in the jet by the floor model at large radii. At large radii the rest-mass density drops off $\propto r^{-2.2}$, so the rest-mass density scaling of $\propto r^{-2.7}$ does not interfere with this. A radial scaling with a power $\lesssim 2.2$ would lead to non-physical results by loading the jet with extra high-velocity material. The internal energy density floor is never reached in the jet due to the shock heating, which keeps $u/\rho_0 > 1$ in the jet. See section 5 for a more detailed discussion.

Our code keeps track of how often the density goes below the floors and how this modifies the conservation of mass, energy, and angular momentum. The floor model contribution is negligible except in the Poynting-dominated jet within $r \lesssim 10r_g$. This injection of mass is a simple ad-hoc model for the mass-loading of the Poynting jet. Beyond $r \approx 10r_g$, the floor is not activated because the accumulated rest-mass is larger than the floor value. Thus, beyond this point the jet is self-consistently evolved strictly within the ideal MHD approximation.

No explicit reconnection model is included. However, our code checks the effective resistivity by measuring the rest-mass flux across field lines. For the boundary between the disk wind and the Poynting-dominated jet, the total rest-mass flux across the field line is negligible compared to the rest-mass flux along the field line determined by the floor model. An unresolved model would load field lines with rest-mass that crosses field lines and not properly represent any physical model of resistivity (McKinney 2004).

This “floor model” prescription was found to give quantitatively similar results to physically-based models of the mass-loading (McKinney 2005c) for which most of the mass-loading takes place only near the black hole for $r \lesssim 10r_g$. Note that McKinney (2005c) performed identical (including random seed for initial condition perturbations) simulations as in this paper except the method used to add mass and energy to the Poynting jet. In this paper, the floor model is chosen to most closely match the physically-based model described in McKinney (2005c). As mentioned there, the results are quantitatively similar except within $r < 10r_g$ and only inside the Poynting jet.

3.3 Lorentz Factors

This paper studies the speed of the jet as determined by the Lorentz factor. The Lorentz factor of the jet can be measured with respect to any frame. We measure the Lorentz factor with respect to a static observer at infinity,

$$\Gamma \equiv u^t = u^t \sqrt{-g_{tt}}, \quad (13)$$

in Boyer-Lindquist coordinates, where no static observers exist inside the ergosphere. This is in contrast to the definition of $W \equiv u^t \sqrt{-1/g^{tt}}$, which is the Lorentz factor as measured by a ZAMO observer as used by many numerical relativists.

Strict upper limits on the Lorentz factor and the angular velocity at large distances can be obtained from the local flow quantities. The Lorentz factor and ϕ -velocity at large distances for an axisymmetric, stationary flow have upper limits of

$$\Gamma_\infty \equiv \frac{-T_t^p}{\rho_0 u^p} = -hu_t + \Phi\Omega_F B_\phi \quad (14)$$

$$u_\infty^\phi \equiv \frac{T_\phi^p}{\rho_0 u^p} = hu_\phi + \Phi B_\phi, \quad (15)$$

where p indicates either poloidal direction (e.g., r or θ), $h \equiv (\rho_0 + u_g + p)/\rho_0$ is the specific enthalpy, $\Phi \equiv B^p/(\rho_0 u^p)$ is the conserved magnetic flux per unit rest-mass flux, $\Omega_F \equiv F_{tp}/F_{p\phi}$ is the conserved field rotation frequency, $B_\phi \equiv F_{\phi t}$ is the covariant toroidal magnetic field, and $u_\infty^\phi \equiv u_{\phi,\infty}$ is the orthonormal angular velocity at large distances. For a stationary, axisymmetric flow, these are the energy and angular momentum flux per unit rest-mass flux that are conserved along flux surfaces. The matter and electromagnetic pieces are separable, such that

$$\Gamma_\infty = \Gamma_\infty^{(\text{MA})} + \Gamma_\infty^{(\text{EM})} \quad (16)$$

$$u_{\phi,\infty} = u_{\phi,\infty}^{(\text{MA})} + u_{\phi,\infty}^{(\text{EM})}. \quad (17)$$

See McKinney (2005b) for more details.

Excluding radiative processes and with some physical accounting of the mass-loading of the jet, the results of this paper suggest one can approximately assume almost all the magnetic and thermal energy go into particle kinetic energy. Thus Γ_∞ and $u_{\phi,\infty}$ may represent the Lorentz factor and angular velocity at large distances before the energy is lost to radiation once the flow is optically thin.

3.4 Units

The units in this paper have $GM = c = 1$, which sets the scale of length ($r_g \equiv GM/c^2$) and time ($t_g \equiv GM/c^3$). The mass scale is determined by setting the observed (model-dependent measured or inferred for GRB-type systems) mass accretion rate (\dot{M}_0) equal to the accretion rate through the black hole horizon as measured in a simulation. So the mass scale is scaled by the mass accretion rate (\dot{M}_0) at the horizon ($r = r_H \equiv r_g(1 + \sqrt{1 - j^2})$), such that $\rho_{0,disk} \equiv \dot{M}_0[r = r_H]t_g/r_g^3$ and the mass scale is then just $m \equiv \rho_{0,disk}r_g^3 = \dot{M}_0[r = r_H]t_g$. For a black hole with angular momentum $J = jGM^2/c$, $j = a/M$ is the dimensionless Kerr parameter with $-1 \leq j \leq 1$.

The results of the simulations can be applied to

any astrophysical system once the value of $\rho_{0,disk}$ is estimated. For example, a collapsar model with $\dot{M} = 0.1\text{M}_\odot s^{-1}$ and $M \approx 3\text{M}_\odot$, then $\rho_{0,disk} \approx 3.4 \times 10^{10} \text{g cm}^{-3}$ (MacFadyen & Woosley 1999). M87 has a mass accretion rate of $\dot{M} \sim 10^{-2}\text{M}_\odot \text{yr}^{-1}$ and a black hole mass of $M \approx 3 \times 10^9 \text{M}_\odot$ (Ho 1999; Reynolds et al. 1996) giving $\rho_{0,disk} \sim 10^{-16} \text{g cm}^{-3}$. GRS 1915+105 has a mass accretion rate of $\dot{M} \sim 7 \times 10^{-7}\text{M}_\odot \text{yr}^{-1}$ (Mirabel & Rodriguez 1994; Mirabel & Rodriguez 1999; Fender & Belloni 2004) with a mass of $M \sim 14\text{M}_\odot$ (Greiner et al. 2001), but see Kaiser et al. (2004). This gives $\rho_{0,disk} \sim 3 \times 10^{-4} \text{g cm}^{-3}$.

4 NUMERICAL SETUP

The GRMHD equations of motion are integrated numerically using a modified version of a numerical code called HARM (Gammie et al. 2003a), which uses a conservative, shock-capturing scheme. Compared to the original HARM, the inversion of conserved quantities to primitive variables is performed by using a new faster and more robust two-dimensional non-linear solver (Noble et al. 2005). A parabolic interpolation scheme (Colella & Woodward 1984) is used rather than a linear interpolation scheme, and an optimal total variational diminishing (TVD) third order Runge-Kutta time stepping (Shu 1997) is used rather than the mid-point method. For the problems under consideration, the parabolic interpolation and third order time stepping method reduce the truncation error significantly, including regions where $b^2/\rho_0 \gg 1$.

4.1 Computational Domain

The computational domain is *axisymmetric*, with a grid that extends from $r_{in} = 0.98r_H$, where r_H is the horizon, to $r_{out} = 10^4r_g$, and from $\theta = 0$ to $\theta = \pi$. Our numerical integrations are carried out on a uniform grid with coordinates: x_0, x_1, x_2, x_3 , where $x_0 = t[\text{Kerr} - \text{Schild}]$, $x_3 = \phi[\text{Kerr} - \text{Schild}]$. The radial coordinate is chosen to be

$$r = R_0 + e^{x_1^{n_r}}, \quad (18)$$

where R_0 is chosen to concentrate the grid zones toward the event horizon (as R_0 is increased from 0 to r_H) and n_r controls the enhancement of inner to outer-radial regions. For studies where the disk and jet interaction is of primary interest, $R_0 = 0$ and $n_r = 1$ are chosen. For this paper, for which in addition the far-field jet is of interest, $R_0 = -3$ and $n_r = 10$ are chosen in order to reach large distances with few grid points and to have the inner-radial computational region resolved similarly to the models of McKinney & Gammie (2004). The θ coordinate is chosen to be

$$\theta = \pi x_2 + \frac{1}{2}(1 - h(r)) \sin(2\pi x_2), \quad (19)$$

where $h(r)$ is used to concentrate grid zones toward the equator (as h is decreased from 1 to 0) or pole (as h is increased from 1 to 2). The jet at large radii is resolved together with the disk at small radii using

$$h(r) = 2 - Q_j(r/r_{0j})^{-n_j g_j} \quad (20)$$

with the parameters of $Q_j = 1.3$, $r_{0j} = 2.8$, $n_j = 0.3$, $r_{1j} = 20$, $r_{2j} = 80$, and

$$g_j = g_j(r) = \frac{1}{2} + \frac{1}{\pi} \tan\left(\frac{r - r_{2j}}{r_{1j}}\right) \quad (21)$$

is used to control the transition between inner and outer-radial regions. The values of Q_j , r_{0j} , n_j , r_{1j} , and r_{2j} were set empirically to approximately follow the simulated jet from the horizon to large distances. An alternative to this fixed refinement of the jet and disk is an adaptive refinement (see, e.g., Zhang & MacFadyen 2005).

The numerical resolution of all the models described is 512×256 compared to the fiducial model with 456^2 in McKinney & Gammie (2004). However, due to the enhanced θ grid, the resolution in the far-field jet region is ~ 10 times larger. Also, with the use of a parabolic interpolation scheme, the overall effective resolution is additionally enhanced. Compared to our previous model this gives us an effective θ resolution of ≈ 9000 zones.

All the results in this paper are robust to changes in numerical resolution, as has been explicitly verified by convergence testing in which the resolution, order of the spatial interpolation, and θ -grid geometry were varied. This included varying the transition radius at which the grid resolution in the jet becomes larger than the disk via different $Q_j = \{1.3, 1.8\}$, using resolutions of 256×256 and 512×256 , and using linear and parabolic spatial interpolation schemes. In all cases, no qualitative differences were found.

4.2 Model Setup

All the experiments performed evolve an initially weakly magnetized torus around a Kerr black hole in axisymmetry. A generic model is used so the results mostly can be applied to any black hole system. The model of the initial disk is identical to the model studied in McKinney & Gammie (2004), and so direct comparisons can be made to our prior work. The new models have an extended radial grid and have a longer duration. These were required to study the large-scale propagation of the Poynting-dominated jet.

A black hole spin of $j = 0.9375$ is chosen, but this produces similar results to models with $0.5 \lesssim j \lesssim 0.99$ (see also, e.g., McKinney & Gammie 2004). This value of the black hole spin is close to the equilibrium black hole spin for a black hole accreting a disk with a height (H) to radius (R) ratio of $H/R \sim 0.26$ (Gammie, Shapiro, & McKinney 2004).

The model is run for $\Delta t = 1.4 \times 10^4 t_g$, which is about 52 orbital periods at the pressure maximum and about 1150 orbital periods at the black hole horizon.

Since the model is axisymmetric, disk turbulence is not sustained after about $t \sim 3000 t_g$ (McKinney & Gammie 2004), after which the anti-dynamo theorem prevails (Cowling 1934). However, while this affects the disk accretion by forcing it to become more “laminar,” this does not affect the evolution of the Poynting-dominated jet. That is, from the time of turbulent accretion to “laminar” accretion, the funnel region is mostly unchanged. Indeed, the far-field jet that has already formed is causally disconnected from the region where the accretion disk would still be turbulent.

4.3 Initial Conditions

The initial conditions consist of an equilibrium torus, which is a “donut” of plasma with a black hole at the center (Fishbone & Moncrief 1976; Abramowicz, Jaroszinski, & Sikora 1978). This torus is a solution to the axisymmetric stationary hydrodynamic equations and is supported against gravity by centrifugal and pressure forces. The solutions of Fishbone & Moncrief (1976) corresponding to $u^t u_\phi = \text{const.}$ are used. The initial inner edge of the torus is set at $r_{\text{edge}} = 6$. The equation of state is a gamma-law ideal gas with $\gamma = 4/3$, but other γ lead to similar results (McKinney & Gammie 2004). The models have $u^t u_\phi = 4.281$, the pressure maximum is located at $r_{\text{max}} = 12r_g$, the inner edge at $(r, \theta) = (6r_g, \pi/2)$, and the outer edge at $(r, \theta) = (42r_g, \pi/2)$. The orbital period at the pressure maximum is $2\pi(a + (r_{\text{max}}/r_g)^{3/2})t_g \simeq 267t_g$, as measured by an observer at infinity. The torus chosen has a disk height (H) to radius (R) ratio of $H/R \sim 0.26$ on average, and is slightly thinner (thicker) at the inner (outer) radial edge.

As done by McKinney & Gammie (2004), a purely poloidal magnetic field is placed into the initial torus. The field can be described using a vector potential with a single nonzero component, and we choose $A_\phi \propto \text{MAX}(\rho_0/\rho_{0,\text{max}} - 0.2, 0)$. The field is therefore restricted to regions with $\rho_0/\rho_{0,\text{max}} > 0.2$. The restriction of the field to be inside the torus is to avoid regions that are numerically estimated to have large magnetic field per unit particle just outside the torus. The field is normalized so that the minimum ratio of gas to magnetic pressure is 100. The equilibrium is therefore only weakly perturbed by the magnetic field.

While the torus is stable to axisymmetric hydrodynamic instabilities, the torus is unstable to global non-axisymmetric hydrodynamic modes (Papaloizou & Pringle 1983). However, when the torus is embedded in a weak magnetic field, the magnetorotational instability (MRI) dominates those hydrodynamic modes (Balbus & Hawley 1991; Gammie 2004). Small perturbations are introduced in the internal energy density, which induces velocity perturbations that seed the instability.

No initial large-scale net vertical field is necessary to drive a Poynting jet, since a large-scale poloidal field is self-consistently generated with the above prescription for the initial field geometry (Hirose et al. 2004; McKinney & Gammie 2004; McKinney 2005a). In addition, other field geometries, such as a net vertical field or multiple field loops within the disk, lead to similar results (McKinney & Gammie 2004). Reconnection efficiently erases the initial geometrical differences (McKinney & Gammie 2004; McKinney 2005a). Only contrived fields without any poloidal component lead to no Poynting jet (De Villiers et al. 2005a). Otherwise, the magneto-rotational instability drives the amplification of toroidal and poloidal flux through differential rotation.

Beyond the disk, we choose two different models of the matter. The first is to set the densities to the “floor model” value (denoted as environment 1). The second is to set the rest-mass density to $\rho_0 = 10^{-4} r^{-3/2} \rho_{0,\text{disk}}$ and the internal energy density to $u = 10^{-6} r^{-5/2} \rho_{0,\text{disk}}$ (denoted as environment 2). In both cases, there is no magnetic field outside the disk. The velocity everywhere is set to be equal to the free-

falling frame. The fiducial model described below focuses on the second model of the surrounding medium, while the first model is used to demonstrate the effect of the existence of an environment on the jet.

4.4 Boundary Conditions

Two different models are chosen for the outer boundary condition. The first model is to use a so-called “outflow” boundary condition, for which all primitive variables ($\{\rho_0, u, \tilde{u}^i, B^i\}$) are projected into the ghost zones while forbidding inflow (associated with environment 1). The second model is to inject matter at some specified rate at the outer boundary, unless there is outflow. For the second model, unless there is outflow the outer boundary is set to inject mass at the free-fall rate with no angular momentum, with a density of $\rho_0 = 10^{-4}r^{-3/2}\rho_{0,disk}$ and $u = 10^{-6}r^{-5/2}\rho_{0,disk}$ (associated with environment 2).

The fiducial model below uses the second model, while the first model is used together with the “floor model” version of the initial conditions in order to investigate the effect of the environment on the jet.

4.5 Astrophysical Applicability of Model

As applied to the collapsar model, the outer grid radius of $r_{out} = 10^4r_g$ corresponds to about 20 presupernova core radii (Woosley & Weaver 1995), $\sim 10^{10}$ km, or about 1/10th the entire star’s radius. As applied to M87, the outer radius of the grid is at 1.4pc. For x-ray binaries, the outer radius of the grid is at 0.001AU.

For the collapsar model, the chosen black hole spin would be achieved in the late phase of jet production (MacFadyen & Woosley 1999). As applied to AGN and x-ray binaries, the results should be approximately applicable to systems with $0.5 \lesssim j \lesssim 0.99$.

The duration of the evolution for the collapsar model is ~ 0.2 seconds, and at the spin chosen would correspond to the late phase of accretion when the Poynting flux reaches its largest magnitude (MacFadyen & Woosley 1999). For the AGN M87 the duration corresponds to ~ 7 years. For the x-ray binary GRS 1915+105 the duration corresponds to ~ 1 second.

The chosen H/R and the extent of the disk are similar to the accretion disk that is expected to form in the collapsar model (MacFadyen & Woosley 1999; Kohri & Mineshige 2002; Kohri et al. 2005). While in AGN and x-ray binary systems an extended disk should be studied, the extent of the disk does not affect the results of the jet produced since the time scale of the simulations are relatively short compared to the outer disks’ accretion time scale, $t \sim 2\pi/(\alpha\Omega_K) \sim 10^5t_g$, where $\alpha \sim 0.01$ and Ω_K is the Keplerian angular frequency. The disk thickness is similar to the disk thickness of radiatively inefficient disk models that are used to represent the disks in some AGN and x-ray binaries during their radiatively inefficient cycle (Narayan & Yi 1995). A study of the effect of disk thickness is left for future work.

The “Bondi-flow” model of the matter beyond the disk (environment 2) can be compared to the collapsar model. This would correspond to the collapsing envelope of a massive star. Presupernova models suggest that the infalling

matter is at about 30% the free-fall rate we have chosen (MacFadyen & Woosley 1999), but this small percent difference is unlikely to significantly affect the jet formation. In addition, the angular momentum of the envelope is not important since the disk is already present in our model and the timescale for adding mass to the disk in an accretion shock is much longer than the duration of the simulation. In collapsar models, the density structure near the equatorial plane varies between $\rho_0 \propto r^{-3/2}$ to $\rho_0 \propto r^{-2}$ and the internal energy is $u \propto r^{-5/2}$ to $u \propto r^{-2.7}$ (MacFadyen & Woosley 1999). This is similar to our model, which is expected since the collapsar model involves mostly spherical collapse. As applied to AGN and x-ray binaries, the second model (environment 2) is a type of Bondi inflow of the surrounding medium.

The fiducial model below uses the second model, while the first model is used together with the “floor model” version of the initial conditions in order to investigate the effect of the environment on the jet.

5 NUMERICAL RESULTS

The overall character of the accretion flow is unchanged compared to the descriptions given in McKinney & Gammie (2004). The disk enters a long, quasi-steady phase in which the accretion rates of rest-mass, angular momentum, and energy onto the black hole fluctuate around a well-defined mean. Beyond $t \sim 3000t_g$, the mass accretion rate drops, but all other quantities in the disk and jet remain similar.

As in McKinney & Gammie (2004), a mildly relativistic wind is launched from the inner edge of the disk with a half-opening angle of roughly 16° to 45° . In this model the disk wind has $\Gamma \sim 1.5$. However, a long temporal study of this disk wind depends on sustaining disk turbulence, which decays beyond $t \sim 3000t_g$ in this axisymmetric model.

The coronal-funnel boundary contains shocks with a sonic Mach number of $M_s \sim 100$. The inner-radial interface between the disk and corona is a site of vigorous reconnection due to the magnetic buoyancy and convective instabilities present there. These two parts of the corona (coronal-funnel wall and inner-radial disk-corona interface) are about 100 times hotter than the bulk of the disk. Thus, these coronal components are a possible sites for Comptonization and nonthermal particle acceleration.

Meanwhile, as in McKinney & Gammie (2004), a Poynting-dominated jet has formed. The Poynting-dominated jet forms as the differential rotation of the disk and the frame-dragging of the black hole induce a significant toroidal field that launches material away from the black hole. The Poynting-dominated jet is launched once the pressure of the mostly nonmagnetic initial funnel material is lower than the toroidal magnetic pressure. This occurs within $t \lesssim 500t_g$.

Figure 1 and figure 2 show the log of rest-mass density and magnetic field at the final time of $t = 1.4 \times 10^4t_g$. Clearly, the jet has pummelled its way through the surrounding medium. By the end of the simulation, the field has been self-consistently launched into the funnel region and has a regular geometry there. The density and field show how the surrounding medium is shocked by the jet in a lateral direction. In the disk and at the surface of the disk the

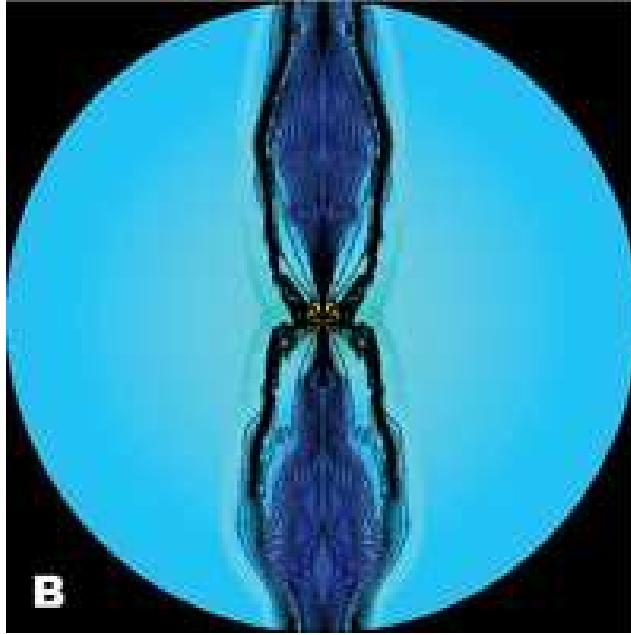
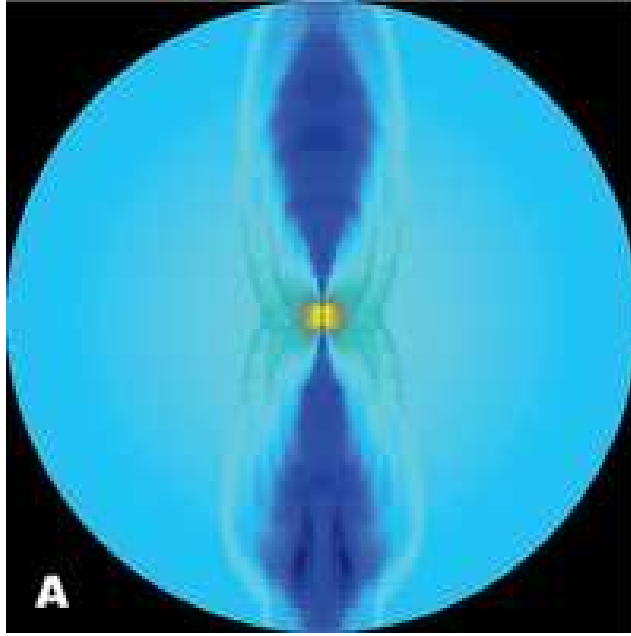


Figure 1. Panel (A) shows final distribution of $\log \rho_0$ on the Cartesian plane. Black hole is located at center. Panel (B) shows magnetic field overlaid on top of \log of density. Outer scale is $r = 10^4 r_g$. Time is $t = 1.4 \times 10^4 t_g$. Color represents $\log(\rho_0 / \rho_{0, \text{disk}})$ with dark red highest and dark blue lowest. The final state has a density maximum of $\rho_0 \approx 2\rho_{0, \text{disk}}$ and a minimum of $\rho_0 \sim 10^{-13} \rho_{0, \text{disk}}$ at large radii. Grid zones are not smoothed to show grid structure. Outer-radial zones are large, but outer θ zones are below the resolution of the figure. For the purposes of properly visualizing the accretion flow and jet, we follow MacFadyen & Woosley (1999) and show both the negative and positive x -region by duplicating the axisymmetric result across the vertical axis.

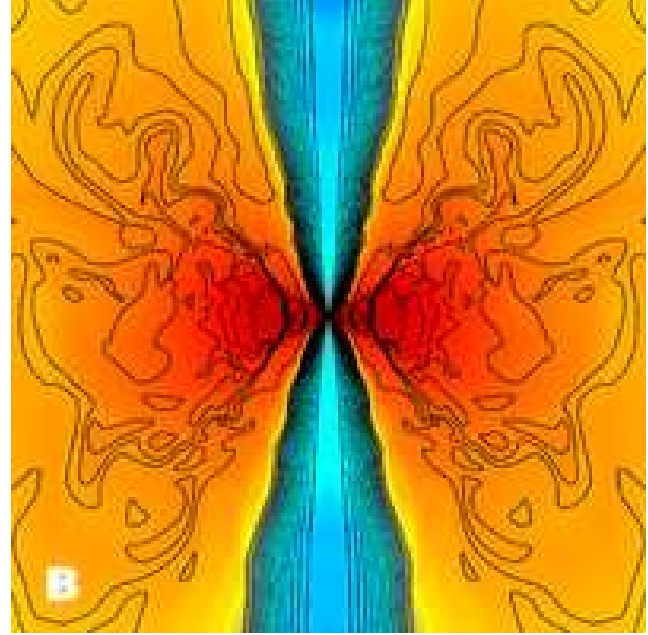
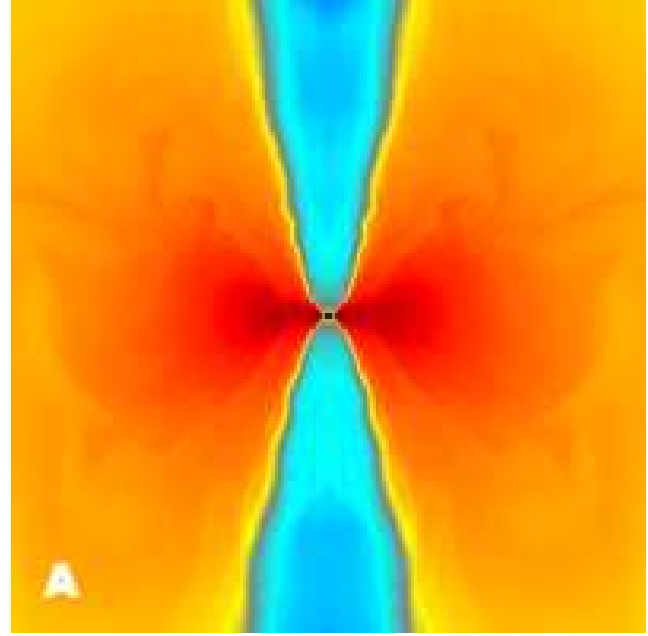


Figure 2. Same as figure 1, but outer scale is $r = 10^2 r_g$.

field is curved on the scale of the disk scale height. Within $r \lesssim 10^2 r_g$ the funnel field is ordered and stable due to the poloidal field dominance. However, beyond $r \sim 10 - 10^2 r_g$ the poloidal field is relatively weak compared to the toroidal field and the field lines bend and oscillate erratically due to pinch instabilities. The radial scale of the oscillations is $10^2 r_g$ (but up to $10^3 r_g$ and as small as $10 r_g$), where $r \sim 10 r_g$ is the radius where poloidal and toroidal field strengths are equal. By the end of the simulation, the jet has only fully evolved to a state independent of the initial conditions out to $r \approx 5 \times 10^3 r_g$, beyond which the jet features are a result

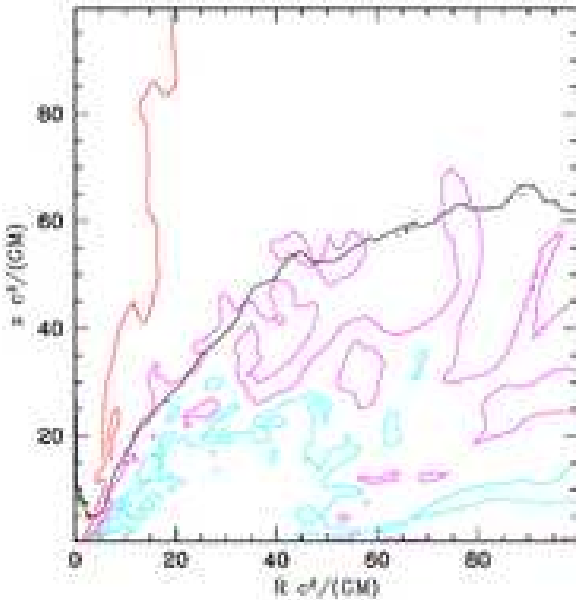


Figure 3. Contours for the disk-corona, corona-wind, and wind-jet boundaries at $t \approx 1500t_g$ and an outer scale of $r \approx 10^2r_g$. The disk-corona boundary is a cyan contour where $\beta \approx u/b^2 = 3$, the corona-wind boundary is a magenta contour where $\beta = 1$, and the wind-jet boundary is a red contour where $b^2/(\rho_0 c^2) = 1$. The black contour denotes the boundary beyond which material is unbound and outbound (wind + jet).

of the tail-end of the initial launch of the field. The head of the jet has passed beyond the outer boundary of $r = 10^4r_g$.

Figure 2 shows that the strongest magnetic field is near the black hole in an X-configuration due to the Blandford-Znajek effect having a power $dP_{jet}/d\theta \propto \sin^2 \theta$ that is truncated by the disk near the equatorial plane.

Figures 3 and 4 show the energy structure of the disk, corona, and jet. This figure is comparable to the left panel of figure 2 in McKinney & Gammie (2004). These plots show the boundaries between the ‘‘disk,’’ ‘‘corona,’’ ‘‘disk wind,’’ and ‘‘Poynting jet.’’ The disk-corona boundary is defined to be where $\beta \equiv p_g/p_b \equiv 2(\gamma - 1)u/b^2 = 3$, the corona-wind boundary is defined to be where $\beta = 1$, and the wind-jet boundary is defined to be where $b^2/(\rho_0 c^2) = 1$. The plot also shows the boundary beyond which material is unbound and outbound (wind and jet), which here is defined as where $u^p > 0$ and $u_t = -1$. This corresponds to where non-interacting *particles* are unbound, although thermal and magnetic energy can further unbind the matter. Hence, more material within the surface is also unbound.

The jet stays collimated, while the disk wind has a large opening angle at large radii. Beyond $r \approx 10r_g$, the jet undergoes poloidal oscillations due to toroidal pinch instabilities. By $r \gtrsim 100r_g$, pinch instabilities subside once magnetic energy is converted into thermal energy, which then supports the jet. Residual slow dense and fast diffuse patches from the instability are present in the jet, such as the slower and cooler dense blob shown at top left corner of figure.

Figure 5 shows the disk, corona, and jet magnetic field structure during the turbulent phase of accretion at $t \approx 1500t_g$. Compared to figure 2, this shows the turbulence in

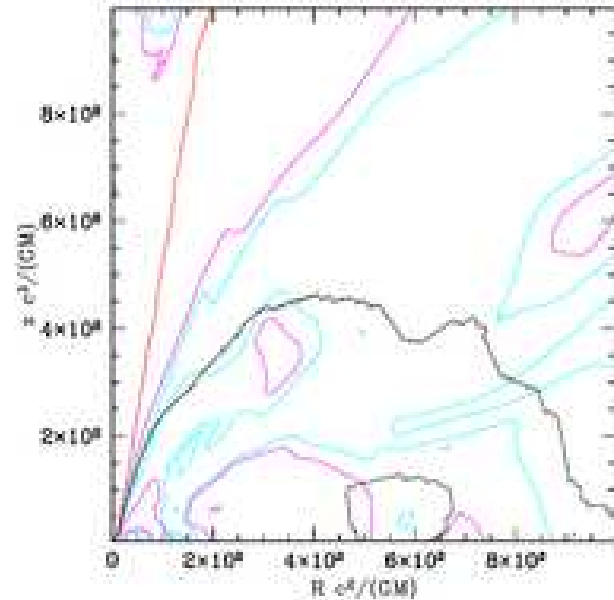


Figure 4. Same as figure 3, but for $t \approx 1.4 \times 10^4 t_g$ and an outer scale of $r \approx 10^3 r_g$. At large scales, the cyan and magenta contours closer to the equatorial plane are not expected to cleanly distinguish any particular structure.

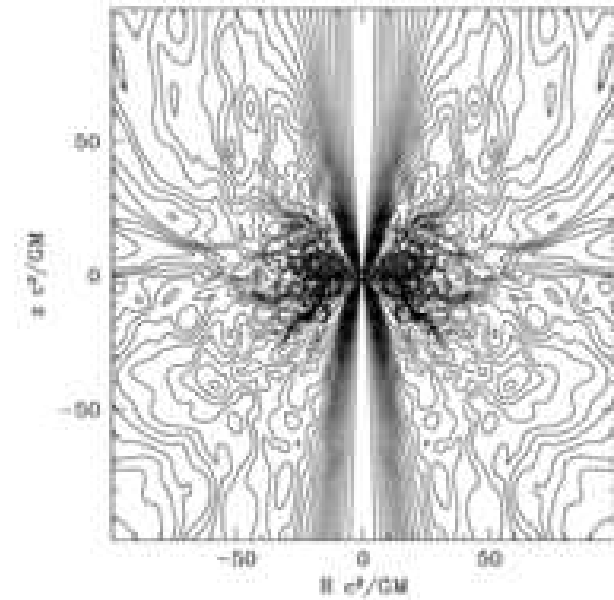


Figure 5. Field geometry near black hole for $t \approx 1500t_g$ during phase of strong disk turbulence.

the disk, but is otherwise similar. The jet, disk, and coronal structures remain mostly unchanged at late times despite the decay of disk turbulence. That is, the current sheets in the disk do not decay and continue to support the field around the black hole that leads to the Blandford-Znajek effect. The coronal thickness and radial extent do not require the disk turbulence, which only adds to the time-dependence of the disk wind. Note that despite the fact that the disk

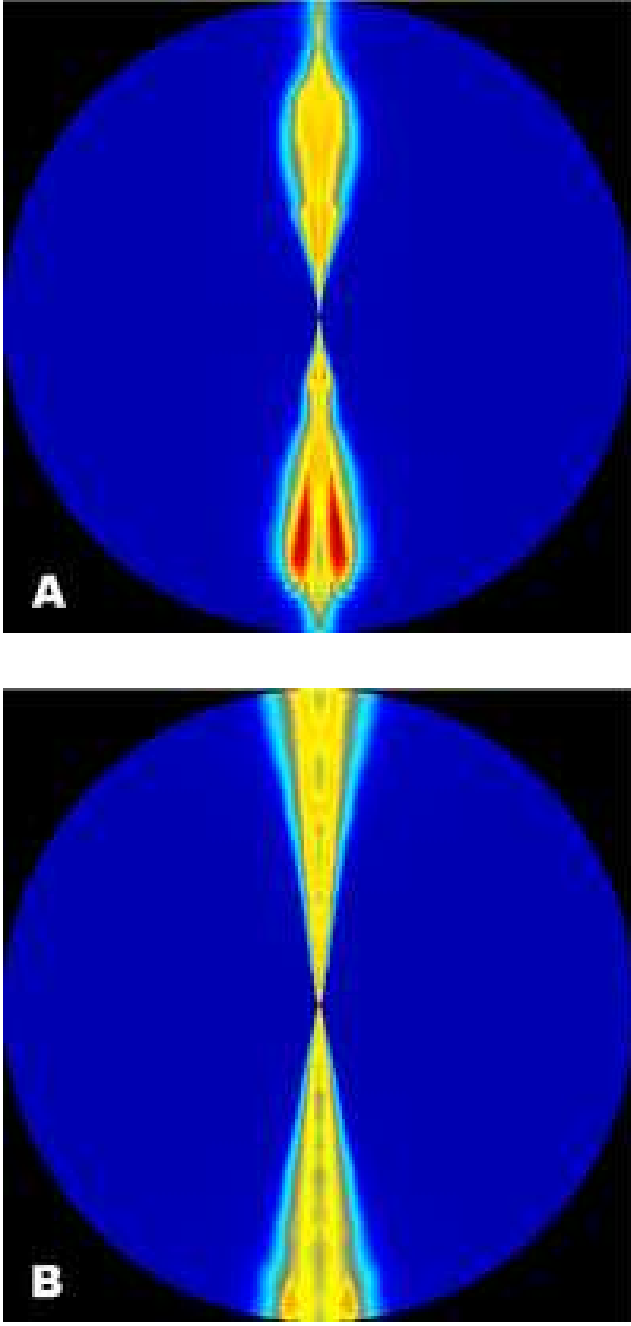


Figure 6. Plot of $\log \Gamma_\infty$ with red highest ($\Gamma_\infty \sim 10^4$) and blue lowest. Yellow is $\Gamma_\infty \sim 10^2 - 10^3$. Panel (A) shows outer scale of $r = 10^4 r_g$, Panel (B) shows outer scale of $r = 10^3 r_g$ with same color scale. Jet is independent of initial conditions by $r \approx 5 \times 10^3 r_g$. Jet becomes conical at large radii with a core half-opening angle $\theta_j \approx 5^\circ$.

wind only contains small-scale magnetic fields, such fields still lead to self-collimation (Li 2002).

Figure 6 shows Γ_∞ , which reaches up to $\Gamma_\infty \sim 10^3 - 10^4$, for an outer scale of $r = 10^4 r_g$ (panel A) and an outer scale of $r = 10^3 r_g$ (panel B). The inner-radial region is not shown since Γ_∞ is divergent near the injection region where the ideal-MHD approximation breaks down. Different real-

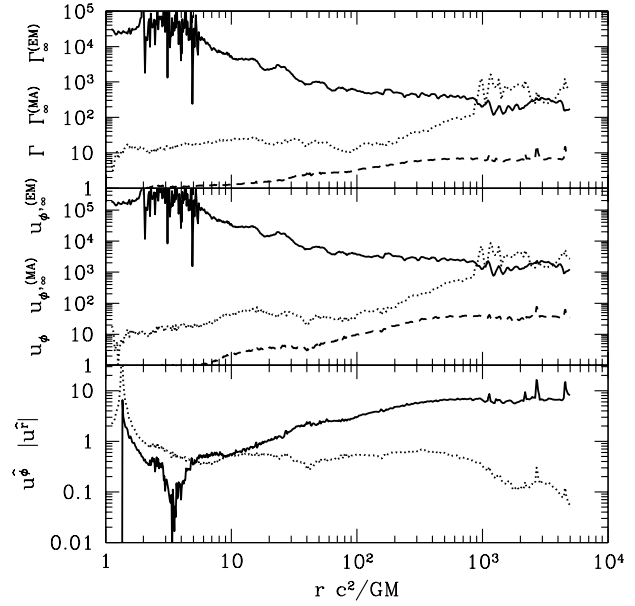


Figure 7. A radial cross section along a mid-level field line in the jet showing the velocity structure. The top panel shows $\Gamma_\infty^{(\text{EM})}$ (solid line), $\Gamma_\infty^{(\text{MA})}$ (dotted line), and Γ (dashed line). The middle panel shows $u_{\phi,\infty}^{(\text{EM})}$ (solid line), $u_{\phi,\infty}^{(\text{MA})}$ (dotted line), and u_ϕ (dashed line). The bottom panel shows $|u_r|$ (solid line) and u_ϕ (dashed line).

izations (random seed of perturbations in disk) lead up to about $\Gamma_\infty \sim 10^4$ as shown for the lower pole in the color figures. This particular model was chosen for presentation for its diversity between the two polar axes. The upper polar axis is fairly well structured, while the lower polar axis has undergone an atypically strong magnetic pinch instability. Various realizations show that the upper polar axis behavior is typical, so this is studied in detail below. The strong hollow-cone structure of the lower jet is due to the strongest field being located at the interface between the jet and the surrounding medium, and this is related to the fact that the BZ-flux is $\propto \sin^2 \theta$, which vanishes identically along the polar axis. It is only the disk+corona that has truncated the energy extracted, otherwise the peak power would be at the equator. As described in the next section, at larger radii the jet undergoes collimation that results in more of the energy near the polar axis.

5.1 Radial Jet Structure

Figure 7 shows the velocity structure of the Poynting-dominated jet along a mid-level field line, which starts at $\theta_j \approx 46^\circ$ on the black hole horizon and goes to large distance, where the funnel region starts at $\theta_j \approx 63^\circ$ on the horizon. The quantities shown are time-averaged values at late-time.

The top panel of figure 7 shows the electromagnetic (EM) energy flux per unit rest-mass flux ($\Gamma_\infty^{(\text{EM})}$), the matter (MA) energy flux per unit rest-mass flux ($\Gamma_\infty^{(\text{MA})}$), and the Lorentz factor as measured by an observer at infinity (Γ). For $2 \lesssim r \lesssim 10$, the value of $\Gamma_\infty^{(\text{EM})}$ is highly oscillatory.

This shows the location of the stagnation surface, where the poloidal velocity $u^p = 0$, is temporally variable. The stagnation surface is, at least, where the ideal-MHD approximation breaks down and thus at any moment the value of $\Gamma_\infty^{(\text{EM})}$ nearly diverges. Notice that while at $r \lesssim 10^3 r_g$ the Poynting flux dominates, the Poynting flux energy is slowly converted into enthalpy flux due to nonlinear time-dependent shock heating. Shocks are expected beyond the magneto-fast surface (see, e.g., Bogovalov & Tsinganos 2005) and here are partially due to pinch instabilities (Eichler 1993; Begelman 1998; Sikora et al. 2005).

For $r \gtrsim 10^3 r_g$, the enthalpy flux and Poynting flux are in equipartition ($\Gamma_\infty^{(\text{MA})} \sim \Gamma_\infty^{(\text{EM})}$) and so an equipartition “magnetic fireball” has formed. The terminal Lorentz factor is of order $\Gamma_\infty \sim 400$ for this choice of flow line. The Lorentz factor by $r \sim 10^4$ is still only $3 \lesssim \Gamma \lesssim 15$, with smaller spatial patches with $\Gamma \sim 25$. For a radiation pressure-dominated and optically thick flow, this implies there will be an extended acceleration region where the magnetic fireball loses energy during adiabatic expansion.

In a narrow region within the core of the jet (not shown in figure 7) within a half-opening angle of $\theta \approx 5^\circ$, the jet accelerates with

$$\Gamma \sim \left(\frac{r}{10r_g} \right)^{0.3}, \quad (\text{inner}) \quad (22)$$

for $10 < r \lesssim 5 \times 10^3 r_g$, after which the initial conditions dominate the flow. Thus $\Gamma \sim 6$ has been reached in the core. The middle and outer angular parts of the jet follow

$$\Gamma \sim \left(\frac{r}{3r_g} \right)^{0.45}, \quad (\text{inner}) \quad (23)$$

for $3 < r \lesssim 10^3 r_g$, after which the field becomes pseudo-conical and there is no sustained acceleration (or the flow even decelerates). Thus, $\Gamma \sim 10$ has been reached. As discussed below, the field is nearly paraboloidal for the radial range over which there is such power-law acceleration. The behavior of $\Gamma(r)$ is in good agreement with an analytic study of acceleration in a paraboloidal field that predicts $\Gamma \propto r^{1/2}$ (Beskin & Nokhrina 2005). Thus our numerical result is consistent with their analytical result.

The next lower panel of figure 7 shows that the electromagnetic angular momentum is converted to enthalpy angular momentum and that there is a conversion to particle angular momentum.

The bottom panel of figure 7 shows the approximate orthonormal radial ($u^\hat{r} \approx \sqrt{g_{rr}} u^r$) and ϕ ($u^\phi \approx \sqrt{g_{\phi\phi}} u^\phi$) 4-velocities in Boyer-Lindquist coordinates, where the approximation being made is that the metric is dominated by the diagonal terms for $r \gtrsim 10r_g$. The radially directed motion becomes relativistic, while the ϕ -component of the 4-velocity becomes sub-relativistic at large distances. However, the fluid and field rotation is still large enough that it may stabilize the jet against $m = 1$ kink instabilities, as shown in the nonrelativistic case (Ouyed et al. 2003; Nakamura & Meier 2004) and analytically in the relativistic case (Tomimatsu et al. 2001).

Figure 8 shows the collimation angle, rest-mass and internal energy densities, ratio of magnetic to rest-mass energy density, toroidal field strength in orthonormal Boyer-Lindquist coordinates, and the pitch angle along a mid-level field line in the Poynting-dominated jet. The field line is

the same as that in figure 7, and now for both poles of the simulation.

The two poles are similar but not necessarily identical. Many simulations that were performed show at least one polar jet develops some pinch instabilities. In the model shown, one side develops very strong instabilities by the end of the simulation. The development of the pinch instability mostly affects the far-radial Lorentz factor (Γ and Γ_∞ — and so densities). The value of Γ is up to 5 times larger in pinched regions than non-pinched regions, while Γ_∞ can be up to a factor 10 times larger in pinched regions compared to non-pinched regions.

In figure 8, for $7r_g \lesssim r \lesssim 100r_g$ there is a region of collimation slightly faster than power-law. For the field line closest to the disk wind starting at $\theta_j \approx 57^\circ$, collimation is nearly a power-law with

$$\theta_j \approx 57^\circ \left(\frac{r}{2.8r_g} \right)^{-0.3} \quad (24)$$

for $r < 120r_g$ and $\theta_j \sim 8^\circ$ beyond. Closer to the polar axis the collimation is faster. For the field line starting at $\theta_j \approx 17^\circ$,

$$\theta_j \propto r^{-0.4}, \quad (25)$$

approximately up to $r \sim 120r_g$ and $\theta_j \sim 5^\circ$ beyond. The inner core for $5 \lesssim r \lesssim 10^3 r_g$ follows $\theta_j \propto r^{-1/2}$, a paraboloidal field. See also discussion related to figure 10.

From a measurement of the forces along and across the field lines within the Poynting jet, the inner-radial collimation is dominated by confinement by the disk+corona, while in the mid-radial range the disk wind collimates the Poynting flow. Far from the disk wind, the internal jet is collimated by internal hoop stresses due to the paraboloidal field. Note that the classical hoop-stress paradigm that jets can self-collimate is not fully tested here, but these results suggest that collimation is in large part due to, or at least requires, the disk and disk wind.

Notice from figure 7 that there is little acceleration beyond $r \sim 10^3 r_g$. It is well known that magnetic acceleration requires field lines to collimate (Eichler 1993; Li 1993; Begelman & Li 1994; Tomimatsu 1994). In a conical flow, the transfer of magnetic energy into kinetic energy is inefficient. As shown in figure 8, after $r \gtrsim 10^3 r_g$ the flow oscillates around a pseudo-conical asymptote with a mean half-opening angle of $\theta_j \sim 5^\circ$. Beyond this radius, the magnetic energy is instead converted to thermal energy. The pseudo-conical asymptote results once the magnetic energy no longer completely dominates the other energy scales and the disk wind no longer helps collimate the flow. The final opening angle should be similar for other black hole spins, as found in prior studies (McKinney & Gammie 2004).

The lower panels of figure 8 show the toroidal field and pitch angle ($\alpha \equiv \tan^{-1}(|B^\hat{r}|/|B^\hat{\phi}|)$), which shows that eventually the toroidal field completely dominates the poloidal field, and the toroidal field remains ordered. The toroidal field within $r \lesssim 390r_g$ is well fit by

$$\frac{B^\phi}{\sqrt{\rho_{0,disk} c^2}} [\text{G}] \approx -0.0023 \left(\frac{r}{390r_g} \right)^{-0.7}. \quad (26)$$

and is otherwise well fit by

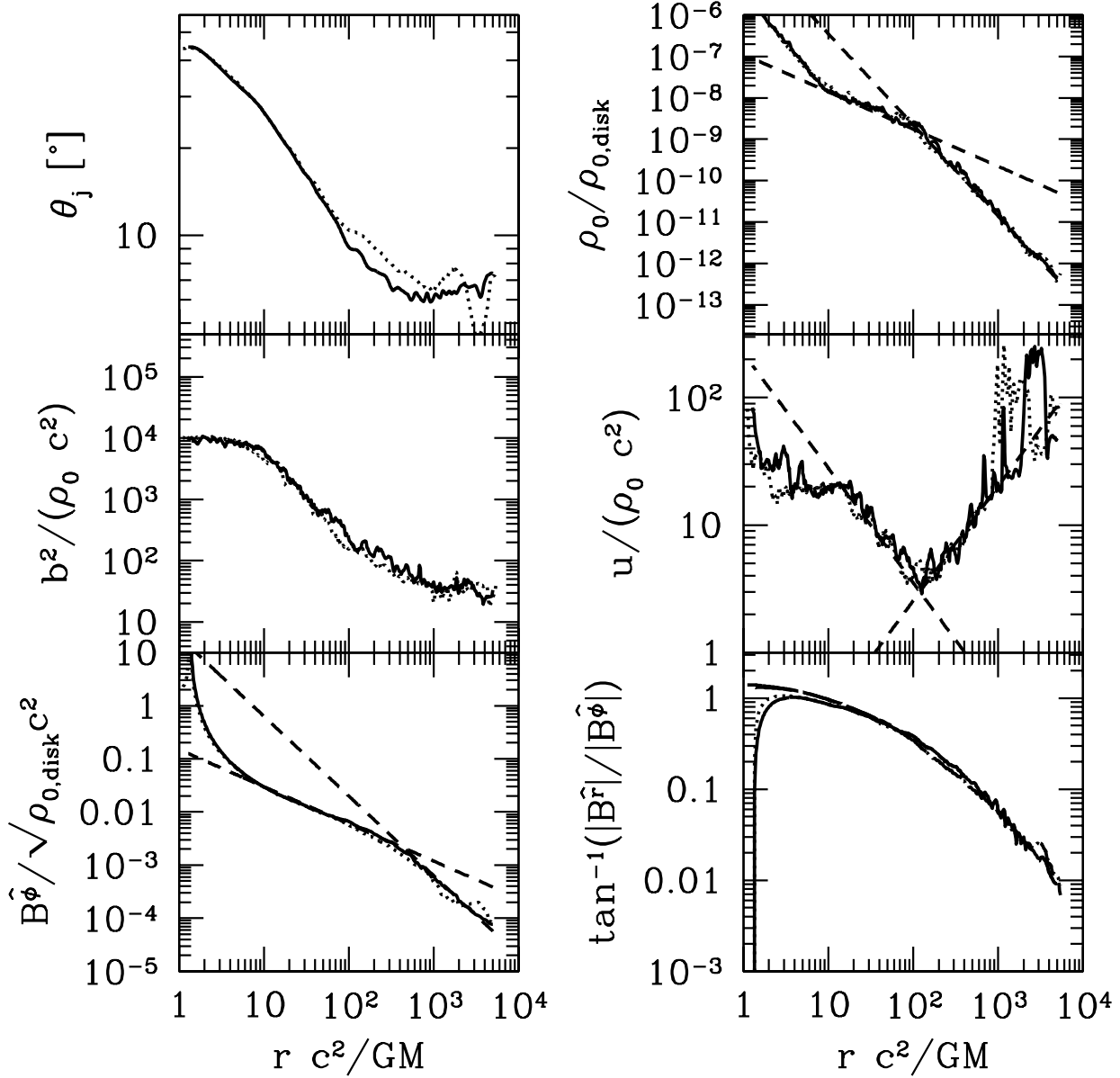


Figure 8. A radial cross-section of both poles (solid and dotted lines) of the jet along a mid-level field line in the jet showing the jet opening angle in degrees, density, and magnetic structure ($B^{\hat{\phi}}$ and $|B^{\hat{\phi}}|$ in Gaussian units). In the density plots and the plot of $B^{\hat{\phi}}$, the overlapping dashed lines are power-law fits. The pitch angle (lower right panel) in Boyer-Lindquist coordinates (which vanishes at the horizon) has an overlapping fit (dash-dotted line) to the Tomimatsu et al. (2001) kink stability criteria when including field rotation.

$$\frac{B^{\hat{\phi}}}{\sqrt{\rho_0, \text{disk}} c^2} [\text{G}] \approx -0.0023 \left(\frac{r}{390 r_g} \right)^{-1.5}. \quad (27)$$

The transition radius is $r \approx 390 r_g$. This transition is associated with the field line going from collimating to not collimating (or slightly decollimating). This is along one mid-level field line, and the coefficients and power laws are slightly different for each field line.

The pitch angle shows that the field becomes toroidally dominated and at large radius the magnetic loops have a pitch angle of $\lesssim 1^\circ$ by $10^3 r_g$. The small pitch-angle suggests that the flow may be kink unstable. The Kruskal-

Shafranov criterion ($|B^{\hat{\phi}}/B^{\hat{r}}| \gtrsim \sqrt{g_{\phi\phi}/g_{\theta\theta}}$), where $\sqrt{g_{\theta\theta}}$ is approximately the vertical length of the jet, is the standard kink instability criterion. However, a self-consistent treatment determined that a Poynting-dominated jet is kink unstable only if both the Kruskal-Shafranov criterion is satisfied and for a mostly radial flow that $|B^{\hat{\phi}}/B^{\hat{r}}| > \sqrt{g_{\phi\phi}}/R_L$ (Tomimatsu et al. 2001), where $R_L = c/\Omega_F$ is the light cylinder radius and cylindrical radius $R \approx \sqrt{g_{\phi\phi}}$ at large distances. Their result only strictly applies inside the light cylinder and for a uniform field, but their result is suggestive of the general result. The lower right panel of figure 8

shows $\tan^{-1}(R_L/\sqrt{g_{\phi\phi}})$ overlapping the pitch angle, and so the flow is marginally stable to the kink instability. Thus, the jet is *not* expected to be (violently) kink unstable if simulated in 3D.

The above discussion implies that the radial magnetic field is well fit by

$$B^{\hat{r}} \approx -\frac{c}{\Omega_F \sqrt{g_{\phi\phi}}} B^{\hat{\phi}}, \quad (28)$$

where we also find that $\Omega_F \approx \Omega_H/2$ is approximately constant along a field line (also see, e.g., McKinney & Gammie 2004), where $\Omega_H = j/(2r_H)$ is the angular frequency of the black hole. The marginal kink stability of our solution is also in concordance with the fact that $\Omega_F \approx \Omega_H/2$ (Tomimatsu et al. 2001), since a Poynting-dominated jet following such a rotation was shown to be marginally kink stable.

As pinch instability-driven oscillations develop, this leads to arbitrarily sized patches moving at arbitrary relative velocities as required by any internal shock model. A patch is simply defined as a localized increase or decrease in various fluid quantities. For example, figure 8 shows that at large radii that the percent difference in the fluctuating part of the opening angle depends on the hemisphere and varies between 10% to 50%. Comparing against each quantity smoothed over a logarithmic interval of $d\log(r) = 0.4$ for the hemisphere with less oscillations, the typical percent difference of quantities along the length of the jet along a mid-level field line is: 10% for ρ_0 , b^2 , $B^{\hat{r}}$, $B^{\hat{\phi}}$, Γ , and u_ϕ ; 20–50% for u ; and 30% for Γ_∞ . The other hemisphere with larger θ_j oscillations has ≈ 5 times the percent difference compared to the first hemisphere. For both hemispheres, the largest several patches have an order unity percent difference. The typical size of a patch is $\sim 100r_g$ to $\sim 10^3r_g$ in the lab frame along the length of the jet.

The top two right panels of figure 8 show the rest-mass density per disk density and internal energy density per rest-mass density. The middle left panel shows the ratio of (twice) the comoving magnetic energy density per unit rest-mass density. The region within $r < 6r_g$ is dominated by the floor model, and this is where the mass is injected into the Poynting-jet. This explains the kink in the density profiles at $r \sim 6r_g$ and the plateau in b^2/ρ_0 . For $r \gtrsim 10r_g$, the floor model is never activated and the matter in the Poynting jet is self-consistently evolved. The inner-radial rest-mass density is well fit by

$$\frac{\rho_0}{\rho_{0,disk}} \approx 1.5 \times 10^{-9} \left(\frac{r}{120r_g} \right)^{-0.9}. \quad (\text{inner}) \quad (29)$$

The outer-radial rest-mass density is well fit by

$$\frac{\rho_0}{\rho_{0,disk}} \approx 1.5 \times 10^{-9} \left(\frac{r}{120r_g} \right)^{-2.2}. \quad (\text{outer}) \quad (30)$$

The transition radius is $r \approx 120r_g$. Likewise, the inner-radial internal energy density is moderately fit by

$$\frac{u}{\rho_{0,disk}c^2} \approx 4.5 \times 10^{-9} \left(\frac{r}{120r_g} \right)^{-1.8}. \quad (\text{inner}) \quad (31)$$

The outer-radial internal energy density is moderately fit by

$$\frac{u}{\rho_{0,disk}c^2} \approx 4.5 \times 10^{-9} \left(\frac{r}{120r_g} \right)^{-1.3}. \quad (\text{outer}) \quad (32)$$

For both the rest-mass and internal energy densities, the transition radius is $r \approx 120r_g$, which is near the transition to a superfast flow. The location of this transition may be due to the thickness of the disk, since the disk leads to collimation at small radii. A flow that collimates more leads to the fast surface closer to the origin (Eichler 1993; Begelman & Li 1994; Tomimatsu 1994). Hence, if a thick disk is required for collimation, then a thick disk is required for a superfast transition at small radii.

The internal energy density stabilizes in value once the equipartition “magnetic fireball” has formed by $r \sim 10^3r_g$. However, the simulation did not extend far enough to guarantee that the equipartition extends for much larger radii. The internal energy may continue to grow, stay in equipartition, or decrease at the expense of adiabatic expansion and acceleration of the jet. The resolution of this issue is left for future work.

5.2 Θ Jet Structure

Figure 9 shows the θ cross-section of the jet at $r = 5 \times 10^3r_g$ for the upper polar axis according to figures 1, 2, and 6. This is the location by which the jet has stabilized in time, where farther regions are still dependent on the initial conditions. The hot fast “core” of the jet includes $\theta \lesssim 5^\circ$ at this radius and is marked by the left dashed vertical line. Also, note that $\theta \approx 8^\circ$ corresponds to the radius obtained for the “mid-level” field line shown for radial cross-sections in figures 7, 8, and 10.

The right dashed vertical line marks the boundary between the last field line that connects to the black hole. This extended angular distribution out to $\theta \lesssim 27^\circ$ is colder than the hot core of the jet. Beyond this region is the surrounding infalling medium. The disk wind has not reached such large radii.

The very inner core of the jet is denser and slower. This feature is simply a result of the fact that the Blandford-Znajek flux is $\propto \sin^2 \theta$. Most of the Poynting energy flux is at the interface between the jet and surrounding medium at small radii, where at larger radii the jet internally evolves to collimate into a narrower inner core where the energy flux is concentrated.

In most of our simulated models, the jet structure is nearly Gaussian. The fiducial model has

$$\epsilon(\theta) = \epsilon_0 e^{-\theta^2/2\theta_\epsilon^2}, \quad (33)$$

where $\epsilon_0 \approx 0.18 \dot{M} c^2$ and $\theta_\epsilon \approx 8^\circ$. The total luminosity per pole is $L_j \approx 0.023 \dot{M}_0 c^2$, where 10% of that is in the “core” within a half-opening angle of 5° with the largest Lorentz factor within the jet. Also, Γ_∞ is approximately Gaussian with

$$\Gamma_\infty(\theta) = \Gamma_{\infty,0} e^{-\theta^2/2\theta_\infty^2}, \quad (34)$$

where $\Gamma_{\infty,0} \approx 3 \times 10^3$ and $\theta_\infty \approx 4.3^\circ$. The Lorentz factor is approximately Gaussian with

$$\Gamma(\theta) = \Gamma_0 e^{-\theta^2/2\theta_\Gamma^2}, \quad (35)$$

where $\Gamma_0 \approx 5$ and $\theta_\Gamma \approx 11^\circ$.

The jet structure can also be modelled by a small uniform core with sharp exponential wings. A good fit is

$$\epsilon(\theta) = 0.1 \dot{M} c^2 \quad (\theta \leq 11^\circ) \quad (36)$$

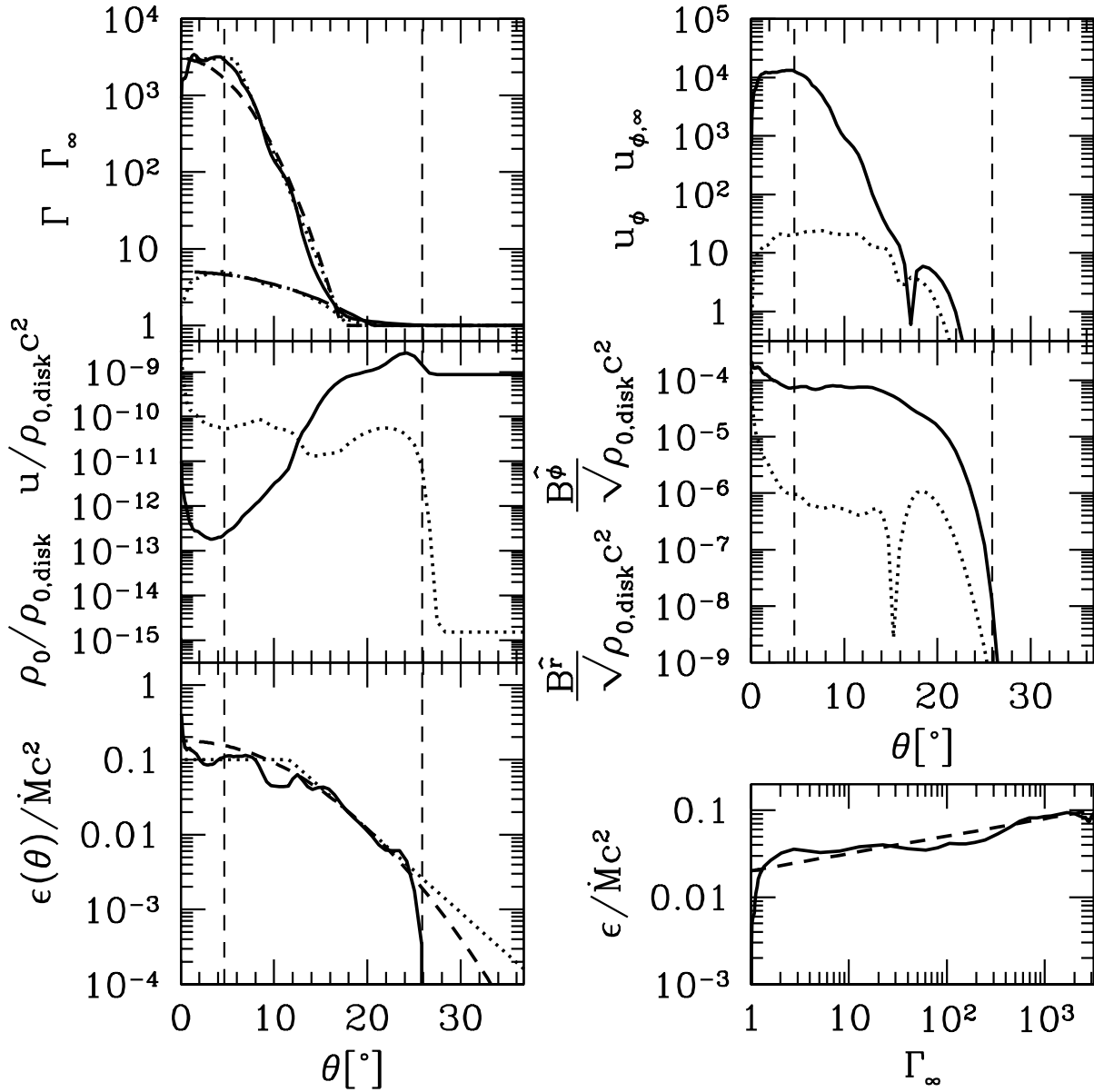


Figure 9. A θ cross-section of the jet at $r = 5 \times 10^3 r_g$ showing the velocity, density, energy, and magnetic structure in Gauss. Γ_∞ and $\epsilon(\theta)/\dot{M}c^2$ have overlapping Gaussian fits (dashed lines) and overlapping uniform+exponential fits (dotted lines), where $\epsilon(\theta) \equiv -r^2 T_t^r \approx r^2 \rho_0 u^r \Gamma_\infty$ (Boyer-Lindquist coordinates). A Gaussian fit to Γ is shown as an overlapping dotted line. Lower right corner shows $\epsilon/\dot{M}c^2$ with overlapping power-law fit (dashed line). The magnetic field components are in Boyer-Lindquist coordinates in an orthonormal basis. Vertical dashed lines marks the outer jet and jet core. Those panels with two separate y-axes labels have the labels vertically ordered by the function value near $\theta = 0$.

and otherwise

$$\epsilon(\theta) = 0.1 \dot{M}c^2 e^{(-3(\theta/\theta_\epsilon - 1))} \quad (\theta \geq 11^\circ), \quad (37)$$

where $\theta_\epsilon = 11^\circ$. We find that

$$\Gamma_\infty = 3 \times 10^3 \quad (\theta \leq 5.8^\circ) \quad (38)$$

and otherwise

$$\Gamma_\infty = 3 \times 10^3 e^{(-4(\theta/\theta_\infty - 1))} \quad (\theta \geq 5.8^\circ), \quad (39)$$

where $\theta_\infty = 5.8^\circ$.

The bottom right corner more clearly demonstrates the fact that there is a significant amount of energy flux at low Lorentz factors. The dependence roughly follows

$$\frac{\epsilon}{\dot{M}c^2} \approx 0.08 \left(\frac{\Gamma_\infty}{10^3} \right)^{1/5}. \quad (40)$$

5.3 Jet Characteristic Structure

In this section the characteristic structure of the jet is considered. First, the ideal MHD dispersion relation is given, e.g., in Gammie et al. (2003a) (there is a sign typo there), and summarized here. In the comoving frame, the dispersion relation is

$$0 = D(k^\mu) \\ = \omega(\omega^2 - k_a^2) \\ \times (\omega^4 - \omega^2 (K^2 c_{ms}^2 + c_s^2 k_a^2/c^2) + K^2 c_s^2 k_a^2), \quad (41)$$

where $k_a \equiv (\mathbf{k} \cdot \mathbf{v}_A)$, $c_{ms}^2 \equiv (\mathbf{v}_A^2 + c_s^2(1 - \mathbf{v}_A^2/c^2))$ is the magnetosonic speed, $c_s^2 \equiv (\partial(\rho+u)/\partial p)_s^{-1}$ is the relativistic sound speed, $\mathbf{v}_A \equiv \mathbf{B}/\sqrt{\mathcal{E}}$ is the relativistic Alfvén velocity, $\mathcal{E} \equiv b^2 + w$, and $w \equiv \rho + u + p$. The invariant scalars defining the comoving dispersion relation are $\omega = -k_\mu u^\mu$, $K^2 = K_\mu K^\mu = k_\mu k^\mu + \omega^2$, where $K_\mu = P_{\mu\nu} k^\nu = k_\mu - \omega u_\mu$ is the projected wave vector normal to the fluid 4-velocity, $\mathbf{v}_A^2 = b_\mu b^\mu/\mathcal{E}$, and $(\mathbf{k} \cdot \mathbf{v}_A) = k_\mu b^\mu/\sqrt{\mathcal{E}}$. The terms in the dispersion relation correspond to, respectively from left to right, the zero frequency entropy mode, the left and right going Alfvén modes, and the left and right going fast and slow modes. The eighth mode is eliminated by the no-monopoles constraint. The dispersion relation gives the ingoing and outgoing slow, Alfvén and fast surfaces.

Energy can be extracted from the black hole if and only if the Alfvén point lies inside the ergosphere (Takahashi et al. 1990). Optimal acceleration of the flow by conversion of Poynting flux to kinetic energy flux occurs beyond the outer fast surface (Eichler 1993; Begelman & Li 1994; Tomimatsu 1994). Other surfaces of interest include: the horizon at $r_H \equiv 1 + \sqrt{1 - j^2}$; the ergosphere at $r \equiv 1 + \sqrt{1 - (j \cos \theta)^2}$; the coordinate basis light surface in where $\sqrt{g_{\phi\phi}} = c/\Omega_F$, where asymptotically $\sqrt{g_{\phi\phi}} = r \sin(\theta)$ is the Minkowski cylindrical radius; and the surface in Boyer-Lindquist coordinates where the toroidal field equals the poloidal field ($|B^\phi| = |B^r|$). Finally, there is a stagnation surface where the poloidal velocity $u^p = 0$. In a field confined jet where no matter can cross field lines into the jet, and if the jet has inflow near the black hole and outflow far from the black hole, then this necessarily marks at least one location where rest-mass must be created either by charge starving the magnetosphere till the Goldreich-Julian charge density is reached (Goldreich & Julian 1969), or pair production rates sustain the rest-mass density to a larger value than the Goldreich-Julian value.

Figure 10 shows θ_j as a function of radius for a field line close to the polar axis, in the middle of the jet, and one close to the outer edge of the jet. Also shown is the Blandford-Znajek paraboloidal solution given by equation 7.1 in Blandford & Znajek (1977). The three paraboloidal field lines correspond to $X(r, \theta)/C = 1.6, 1.2, 0.75$ in that equation, where $X(r, \theta)/C = 2(1 - \log(2))$ along the polar axis. Note that at large radii that a paraboloidal field has $\theta_j \propto r^{-1/2}$, cylindrical has $\theta_j \propto r^{-1}$, and conical has $\theta_j \propto r^0$. The ingoing fast point is nearly coincident with the horizon. The stagnation points have time-dependent positions that vary within approximately $\pm 30\%$ differences.

Notice from figure 10 that the field near the horizon is nearly monopolar. After the stagnation point the field line becomes nearly paraboloidal up to the outgoing

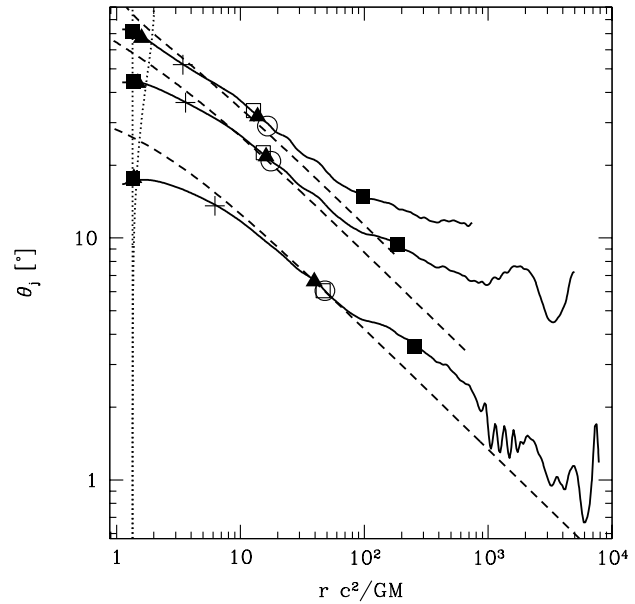


Figure 10. A radial cross-section of the Poynting-dominated jet along three field lines showing the opening angle in degrees. The field lines are close to the polar axis, along a mid-level field line, and close to the outer edge of the Poynting-dominated jet. Overlapping dashed lines are paraboloidal fits within the radial range that has a similar collimation. Solid squares mark the ingoing/outgoing fast points. Solid triangles mark the ingoing/outgoing Alfvén points. Pluses mark the stagnation point. Open squares mark where poloidal and toroidal fields are equal. Open circles mark the light surface. Dotted lines mark the horizon and ergosphere. The field lines at larger θ are shown for a shorter radius due to limitations of a program used to extract a field line contour.

Alfvén point. Beyond this point, the field is unstable to pinch modes and some of the magnetic energy is converted to thermal energy. For the outer and mid-level field lines, after the flow passes through the outgoing fast point, the flow goes from nearly paraboloidal to nearly conical. The inner-level field line continues to follow a fairly paraboloidal collimation with mild oscillations. The magnetic surfaces are therefore paraboloidal in the core of the jet and surrounded by conical surfaces, which is quite similar to the assumed structure of the analytical model by Tomimatsu & Takahashi (2003).

Figure 11 shows the characteristic structure of the jet for one polar axis. The Alfvén surface lies inside the ergosphere, as required to extract energy (Takahashi et al. 1990). Clearly the field lines follow nearly a power-law until $r \sim 10^2 r_g$. The stagnation surface is time-dependent but stable. Clearly the transition to a supercritical (superfast) flow has occurred. After the fast surface, the field lines stretch out and oscillate around a conical asymptote. The fast surface near the polar axis is at $r \sim 250 r_g$, where for the other hemisphere it is at $r \sim 500 r_g$. Other features are quantitatively similar.

Despite the unsteady nature of the flow, the characteristic structure is quite simple and relatively smooth in appearance. This indicates that the flow is mostly stationary. The region near $r \sim 10^4 r_g$ is still determined by the initial conditions, which explains the distorted appearance

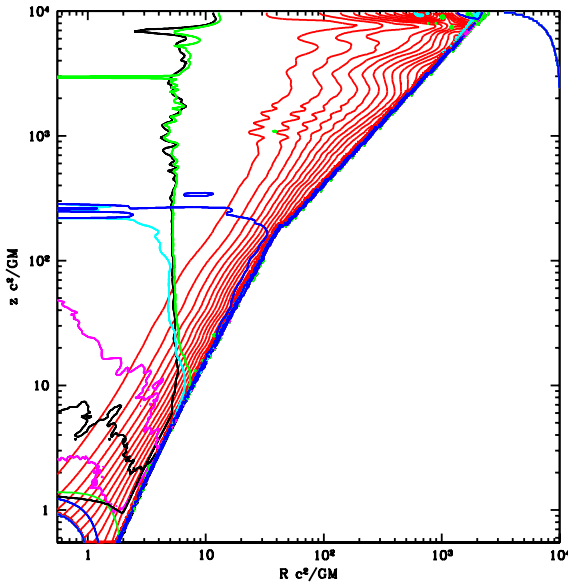


Figure 11. Poynting-dominated jet characteristic (and other) surfaces. Shows a log-log plot of one hemisphere of the time-averaged flow at late time. In such a log-log plot, 45° lines correspond to lines of constant θ . Lines of constant spherical polar r are horizontal near the z -axis and vertical near the R -axis. The field lines are shown as red lines. From $r = 0$ outwards: Blue#1: horizon + ingoing-fast ; Cyan#1: ingoing-Alfvén ; Black#1: $|B^\phi| = |B^r|$; Green#1: ergosphere ; Purple#1: ingoing-slow ; Black#2: stagnation surface where poloidal velocity $u^p = 0$; Purple#2: outgoing-slow ; Cyan#2: outgoing-Alfvén ; Black#3: $|B^\phi| = |B^r|$ again ; Green#2: light cylinder ; Blue#2: outgoing-fast. The disk and coronal regions have been truncated with a power-law cutoff for $r \lesssim 100r_g$ and a conical cutoff for larger radii. Within $r \lesssim 10r_g$ the plotting cutoff creates the appearance that the fast surface and other lines terminate along the cutoff.

of the field lines and other artifacts related to the flow being unsteady.

5.4 Dependence on Surroundings

The jet structure that emerges from the simulation is primarily due to the internal evolution of the jet rather than by the interaction with the surrounding medium. In particular, these GRMHD-based results are insensitive to the two different models of the initial surrounding medium. One model is a surrounding infall of material and the other is an ‘‘evacuated’’ exterior region, as discussed in sections 4.3 and 4.4. The Poynting-dominated jet structure is negligibly broader or narrower in the evacuated case due to magnetic confinement. The disk wind itself also easily plows through the exterior region.

This is in stark contrast to the simulations of relativistic *hydrodynamic* jets (Aloy et al. 2000; Zhang, Woosley, & MacFadyen 2003; Zhang W. et al. 2004), where they find that the environment is primarily responsible for collimating the hydrodynamic flow and hydrodynamic collimation shocks help diminish the mixing between the jet and the surrounding medium. In the

GRMHD case, we find that the confinement is mostly magnetic¹.

The radial structure of the jet is also unaffected by the environment. For example, one can compare the radial structure of the density in the jet (equations 29 and 30) to the density of the evacuated environment model of the surroundings,

$$\frac{\rho_0}{\rho_{0,disk}} = 2 \times 10^{-13} \left(\frac{r}{120r_g} \right)^{-2.7}, \quad (\text{Environment1}) \quad (42)$$

or to the pre-existing spherical infall environment model of the surroundings,

$$\frac{\rho_0}{\rho_{0,disk}} = 8 \times 10^{-8} \left(\frac{r}{120r_g} \right)^{-1.5}. \quad (\text{Environment2}) \quad (43)$$

Even with the drastic difference in rest-mass and internal energy densities, all the results of the Poynting-dominated jet are quantitatively similar. This is much different than the results from hydrodynamic simulations mentioned above.

6 DISCUSSION

We find that the Poynting-dominated jet accelerates to $\Gamma \sim 10$ along nearly paraboloidal field lines. The maximum terminal Lorentz factor is $\Gamma_\infty \lesssim 10^3$, sufficiently relativistic to account for any relativistic jet from GRBs, AGN, or x-ray binaries. At large radii, about half of the energy in the jet is thermal. Thus, for optically thick flows that are radiation-dominated, thermal adiabatic expansion is expected to lead to an extended acceleration range far beyond $r \sim 10^4r_g$. For optically thin flows that are radiation-dominated, much of this energy can be directly released as radiation. In the limit that the radiative time-scale is much shorter than the jet propagation time-scale, the terminal Lorentz factor is limited to $\Gamma_\infty \sim \Gamma \sim 10$.

The part of the jet with the largest energy flux collimates from a half-opening angle of $\theta_j \sim 60^\circ$ near the black hole to $\theta_j \sim 5^\circ$ at large distances. The core of the jet follows nearly paraboloidal field lines for all radii and accelerates with approximately $\Gamma \propto r^{0.3}$ from $r \approx 10r_g$ out to $r \approx 5 \times 10^3r_g$, after which the initial conditions dominate the flow. Thus the core moves with $\Gamma \approx 6$ and may continue to accelerate since the field is still collimating by the outer radius. The middle and outer angular parts of the jet follow nearly paraboloidal lines inside the fast surface and conical lines outside the fast surface. The middle and outer parts follow $\Gamma \propto r^{0.45}$ from $r \approx 3r_g$ up to the point where the flow becomes conical at $r \sim 10^2r_g - 10^3r_g$. Thus these parts move with $\Gamma \sim 10$. The acceleration nearly follows the result from analytic models with exactly paraboloidal field lines that found $\Gamma(r) \propto r^{1/2}$ (Beskin & Nokhrina 2005). That the acceleration found is slightly weaker than for paraboloidal lines is consistent with the fact that the simulated field lines end up not as strongly collimated as paraboloidal.

¹ There is a difference between magnetic confinement and magnetic collimation. Confinement refers to the magnetic field containing the mass of the jet since there is no hydrodynamic mixing, while collimation refers to modifications of the field line geometry along the jet.

The jet structure is Gaussian-like, so there is a non-negligible amount of energy at large angles out to $\theta_j \sim 27^\circ$. This may explain the observations of some GRBs that appear to have a narrow ultrarelativistic component that produces the γ -rays and early afterglow and a wide, mildly relativistic component that produces the radio and optical afterglow (Berger et al. 2003). The provided fits to the jet structures can be folded into various models, such as the probability of observing polarised emission in Compton drag emission models (Ghisellini et al. 2000; Lazzati et al. 2004) or whether Compton-drag models work. Consider the region within $\theta \lesssim 27^\circ$. This is an expanded, relatively cold slow portion of the jet. It is possible that the gamma-ray burst photons are due to Compton drag from soft photons emitted by this jet ‘sheath’ dumping into the faster spine (Begelman & Sikora 1987; Ghisellini et al. 2000; Lazzati et al. 2004).

6.1 Toroidal Field Instabilities

Internal shocks and magnetic instabilities have both been invoked to explain emission from jets associated with GRBs, AGN, and x-ray binary systems. We find that the Poynting-dominated jet becomes unstable beyond the Alfvén surface and magnetic energy is converted to thermal energy. Unlike during reconnection, this process involves toroidal field instabilities that lead to a conversion of magnetic to lateral kinetic energy. These oscillations drive waves into the jet that steepen into shocks and lead to $\Gamma_\infty^{(MA)} \sim 10^3$. This process is consistent with expectations of current-driven instabilities (Eichler 1993; Begelman 1998; Sikora et al. 2005). These instabilities lead to slightly faster and slower moving patches of jet material. Thus, the variability within the jet is dominated by toroidal field instabilities.

Toroidal field instabilities have been invoked to significantly lower the BZ power output (Li 2000), although their estimate was based upon the Kruskal-Shafranov criteria for kink instability, a nonrelativistic model, and limited the BZ power output in the context of an acausal astrophysical load at large distances. At best their estimate determines a limitation of the Poynting flux domination of the jet, but not the total jet power or power emitted by the black hole. Kink instabilities have also been invoked to destroy the coherent structure of jets (for a discussion, see, e.g., Appl 1996), and such instabilities are often regarded as sufficiently strong so that magnetic confinement is not possible (Miller-Jones et al. 2006). However, the Kruskal-Shafranov criteria for kink instability is a necessary but not sufficient condition for kink instabilities to occur, where rotation of the fluid or field lines can stabilize the jet (Tomimatsu et al. 2001).

Blandford-Znajek type jet solutions naturally sit near marginal kink stability (Tomimatsu et al. 2001). Since we find that the self-consistently simulated Poynting jet only marginally satisfies the necessary and sufficient conditions for kink instability, the jet is not expected to be (violently) kink unstable if simulated in full 3D. This explains why astrophysical jets can go to large distances even if satisfying the Kruskal-Shafranov kink criteria.

Internal shocks are expected to generate some of the emission in GRBs, AGN, and x-ray binaries. In the simulated jet, the patches generated by the toroidal field insta-

bilities move at large relative Lorentz factors, and so these patches can lead to internal shocks. However, by the radius simulated, the Lorentz factor is not yet large enough for the standard GRB internal shock model to be efficient (Kobayashi et al. 1997; Mészáros 2002; Ghirlanda et al. 2003; Piran 2005). However, the energy provided by the BZ-driven jet may be more than sufficient to allow for inefficient shocks, since in section 5.2 we found that $L \approx 0.023\dot{M}_0c^2 \sim 4 \times 10^{51} \text{ erg s}^{-1}$ for the collapsar model rather than the canonical $\sim 10^{50} \text{ erg s}^{-1}$ for cosmological GRBs. The acceleration region and internal shock region was not simulated since the dynamical range required is another ~ 6 orders of magnitude in radius.

Toroidal field instabilities have been suggested to generate shocks and high-energy emission in quasar jet systems (Sikora et al. 2005). For GRB systems, if magnetic dissipation continued beyond the γ -ray photosphere at $r \sim 10^7 - 10^8 r_g$, then those shocks could be directly responsible for the γ -ray emission (Lyutikov & Blackman 2001; Lyutikov & Blandford 2003). This single magnetic dissipation model could unify GRB and Blazar emission. This paper does not resolve the emission mechanism, but the results can be used to test the plausibility of emission models.

Some GRB models assume the Poynting energy to be converted into radiation far from the collapsing star by internal dissipation (see, e.g., Thompson 1994; Mészáros & Rees 1997; Spruit, Daigne, & Drenkhahn 2001; Drenkhahn 2002; Drenkhahn & Spruit 2002; Sikora et al. 2003; Lyutikov, Pariev, & Blandford 2003) such as driven by magnetic reconnection. Kink instabilities have been invoked to allow reconnection-driven magnetic energy to be converted into thermal energy to accelerate the flow (Drenkhahn 2002; Drenkhahn & Spruit 2002), although the reconnection rate assumed in those papers is not supported by the GEM project on reconnection (Shay et al. 2001). Some simplified acceleration models assume that kink instabilities drive reconnection that leads to acceleration (Giannios & Spruit 2006). However, despite the simulated jet being marginally stable to current-driven instabilities, significant internal dissipation occurs already by $10^3 r_g$. Reconnection is not likely nor required. The shocks driven by these moderate instabilities are an alternative to the reconnection paradigm.

We find that after these toroidal field instabilities equalize the magnetic and thermal energy at $r \sim 10^3 r_g$ that the jet becomes conical for the angular regions with $\theta_j \gtrsim 5^\circ$. Consequently, this part of the jet ceases to magnetically accelerate beyond this radius. In contrast, the core of the jet within $\theta_j \approx 5^\circ$ remains paraboloidal along the entire jet out to $r \sim 10^4 r_g$. This core may continue to magnetically accelerate beyond this radius. This suggests that toroidal field instabilities play a crucial role in determining the opening angle and terminal Lorentz factor of jets.

Theoretical studies of ideal MHD jets focused on cold jets and the conversion of Poynting energy directly to kinetic energy (see, e.g., Li et al. 1992; Eichler 1993; Begelman & Li 1994; Tomimatsu 1994; Daigne & Drenkhahn 2002; Beskin & Nokhrina 2005). Indeed, much of the work has focused on self-similar models, of which the only self-consistent solution found is suggested to be R-self-similar models (Vlahakis 2004; Fendt & Ouyed 2004). Unfortunately, such models result in only cylindrical

asymptotic solutions, which is apparently not what is observed in AGN jets nor present in the simulations discussed in this paper. The previous section showed that some aspects of the jet are nearly self-similar and that there is some classic ideal-MHD acceleration occurring in this region. However, cold ideal-MHD jet models have no way of addressing the region where magnetic energy is converted to thermal energy in shocks. This region also involves relatively rapid variations in the flow, so stationary jet models would have difficulty modelling this region.

6.2 Simulations as Applied to AGN and X-ray Binaries

Quantitatively all of these results can be rescaled by density in the jet in order to approximately apply to any GRB model and to AGN and x-ray binary systems. This is because the jet has only reached about $\Gamma \sim 10$, which is not too small or large a Lorentz factor, and $\Gamma_\infty \propto 1/\rho_{0,jet}$. Some astrophysical implications of the jet simulations and results as applied to AGN are described in the next several paragraphs, while a detailed discussion of the results as applied to GRBs will be considered in a separate paper.

The angular structure of the simulated jet may help explain many aspects of observed jets. The fast spine can lead to strong Compton scattering of photons to higher energy, while the outer angular part of the jet can lead to radio emission. This process may be required to explain high- and low- energy emission from TeV BL Lac objects and radio galaxies (Ghisellini et al. 2005) and may help explain high-energy observations of blazars (Blandford & Levinson 1995; Ghisellini & Madau 1996; Chiaberge et al. 2000). The full opening angle of $\sim 10^\circ$ of the simulated jet core also agrees with the observations of the far-field jet in M87 (Junor et al. 1999).

The radial structure of the jet and the presence of shocks beyond the Alfvén surface suggest that synchrotron emission should be observed at hundreds of gravitational radii from the black hole rather than near the black hole. This suggests the shock zone (or “blazar zone” for blazars) should be quite extended between $r \sim 10^2 r_g$ and up to about $r \sim 10^4 r_g$ (see, e.g., Sikora et al. 2005). It is also often assumed that if the jet is highly collimated that it is also highly relativistic near the black hole, which would suggest Comptonization of disk photons should produce clear spectral features (Sikora & Madejski 2000). However, the jet may rather accelerate slowly but collimate quickly, which is what we find. There is an early transfer of Poynting flux to kinetic energy flux leading up to about $\Gamma \sim 5 - 10$ by about $r \sim 10^3 r_g$. This is consistent with the lack of observed Comptonization features in blazars (see, e.g., Sikora et al. 2005). At large distances the field becomes toroidally dominated, but this does not necessarily contradict observations of parallel fields in FRI sources (Blandford 2000; Sauty et al. 2002).

Prior work suggested that the BZ power is insufficient to account for Blazar emission (Maraschi & Tavecchio 2003), where they assumed that $\Gamma \sim 10$ and $\theta_j \sim 15^\circ$. However, we find that the structure of the Poynting-dominated jet is nontrivial. The region with $\Gamma \sim 10$ is narrower with $\theta_j \sim 5^\circ$ and jet emission may be dominated by shock accelerated electrons with thermal $\Gamma^{(MA)} \sim \Gamma \gtrsim 100$ with an extended

high energy tail. This lowers the necessary energy budget of the jet enough to be consistent with BZ power driving the jet.

The disk wind may play a crucial role independent of the jet. For example, relatively thin disks or slowly rotating black holes would produce disk winds that could appear as “aborted jets” (Ghisellini et al. 2004). The classical AGN unification models (Urry & Padovani 1995) invoke a dominant role for the molecular torus and broad-line emitting clouds, while the broad disk wind composed of magnetized blob-like regions may significantly contribute to modifications and in understanding the origin of the clouds (Elvis 2000; Elvis et al. 2004).

Erroneous conclusions could be drawn regarding the jet composition since there is actually a jet and disk wind, which could each have a separate composition. That there can be two separate relativistic jet components makes it difficult to draw clear conclusions regarding the composition (Guilbert et al. 1983; Celotti & Fabian 1993; Levinson & Blandford 1996; Sikora & Madejski 2000). Entrainment, which could occur at large distances when the ideal MHD approximation breaks down, also causes difficulties in isolating the “proper” jet component’s composition. In cases where only electron-positron pair jets can be supported, then this would indicate that disk winds are ruled out for such sources, such as recently suggested for FRII sources (Kino & Takahara 2004).

6.3 Disk Winds vs. Poynting Jets in M87

M87 is associated with the most widely studied AGN jet, so here we discuss implications of our results for M87 specifically. Junor et al. (1999) and Biretta et al. (1999, 2002) suggested that M87 slowly collimates from a full opening angle of about 60° near the black hole to 10° at large distances. However, some of their assumptions are too restrictive. First, they assumed the jet is always conical, which is apparent from figure 1 in Junor et al. (1999). If the jet is not conical this can overestimate the opening angle close to the core (i.e. perhaps 35° is reasonable all the way into the core). Second, their beam size was relatively large so that factors of 2 error in the collimation angle are possible. Third, they assumed the radio core is the location of the black hole, while the inner-jet may be cold and only produce synchrotron emission once shocks develop. Finally, the assumption that the jet is a single, slowly collimating jet remains the prevailing view (see, e.g., Tsinganos & Bogovalov 2005; Gracia et al. 2005). GRMHD numerical simulations of jet and disk wind formation suggest that a model with a single jet is too simple of an interpretation of the observations. If there is a highly collimated relativistic Poynting jet surrounded by a weakly collimated disk wind, then this would also fit their observations without invoking slow collimation.

A form of the idea that winds are coincident with, and collimate, jets has also been proposed by Tsinganos & Bogovalov (2005) and applied to M87, but they considered a model where the wind slowly collimates the jet in order to fit observations. Here we suggest that the observations may have been misinterpreted due to the presence of two components: a well-collimated relativistic cold Poynting jet and a mildly relativistic disk wind. We suggest the broader emission component could be due to the disk wind.

More recent maps of the M87 jet formation region showed no “jet formation” structure (Krichbaum et al. 2004). Thus, the structures seen previously may be transient features, such as associated with turbulent accretion disk producing a dynamic disk wind or associated with time-dependent shocks produced in the jet far from the black hole.

Measurements of the apparent jet speed in M87 reveal typically $\Gamma \sim 1.8$ near the core while $\Gamma \sim 6$ at larger radii. However, some core regions are associated with $\Gamma \sim 6$ that rapidly fade (Biretta et al. 1999). This is consistent with a two-component outflow where the cold fast moving core of the jet is only observed if it interacts with the surrounding medium, the slower disk wind, or it undergoes internal shocks.

6.4 Comparisons with Other Numerical Work

Numerical models of jets continue to be studied using the hydrodynamic approximation (MacFadyen & Woosley 1999; Aloy et al. 2000, 2002; Scheck et al. 2002; Zhang, Woosley, & MacFadyen 2003; Zhang W. et al. 2004; Aloy et al. 2005), despite the presence of dynamically important magnetic fields in the accretion disks that have been shown to lead to strongly magnetized jets (De Villiers, Hawley, & Krolik 2003; McKinney & Gammie 2004; De Villiers et al. 2005a). These hydrodynamic studies have suggested that hydrodynamic mixing within the jet may lead to observational signatures in the emission variability. Other models suggested that such hydrodynamic mixing leads to an inability to clearly distinguish the jet composition as either leptonic or baryonic (Scheck et al. 2002). We suggest magnetic instabilities due to pinch or kink modes dominate the variability rather than hydrodynamic instabilities, which are known to be quenched by magnetic confinement (see, e.g., Clarke et al. 1986; Lind et al. 1989; Appl & Camenzind 1992; Rosen et al. 1999). The magnetic confinement severely limits the mixing between the jet and the environment.

Hydrodynamic studies have suggested that shocks driven into the surrounding environment collimate the jet (Aloy et al. 2000; Zhang, Woosley, & MacFadyen 2003; Zhang W. et al. 2004). We find that the jet structure is negligibly broader for models with a negligible surrounding environment. This is because the jet is magnetically confined and collimated at large radii. As applied to GRBs, our results suggest that the presence of an extended stellar envelope plays no role in the jet dynamics except to provide the disk with material. However, the jet plays a significant role in modifying the stellar envelope by sending lateral shocks through the star.

Similar studies have also suggested that variations in the Lorentz factor are due to hydrodynamic effects (Aloy et al. 2002, 2005), but we find that variations in the Lorentz factor are due to magnetic instabilities. Unlike their models, our models generate a relatively simple jet structure that can be fit by a Gaussian or top-hat + exponential wings. Once the shock heating generates an equilibrium magnetic fireball, the internal thermal support and toroidal magnetic confinement keep the jet stable and conical out to large distances. For an optically thick flow like in GRB jets, the flow should convert the thermal energy to kinetic energy in adiabatic expansion and lead to $\Gamma \sim 10^3$.

For hydrodynamic models of GRBs, energy is injected to model the annihilation of neutrinos (Aloy et al. 2000; Zhang, Woosley, & MacFadyen 2003; Zhang W. et al. 2004). They assumed a highly relativistic jet is formed early near the black hole and they injected the matter with a large enthalpy per baryon of about $u/\rho_0 c^2 \sim 150$. They tuned the injected energy to have their results agree with observations (Frail et al. 2001). Other models with a disk and jet find that $u/\rho_0 c^2 \sim 10$, which is suggested to imply that $\Gamma_\infty \sim 10$, insufficient for GRBs (MacFadyen & Woosley 1999), see their figure 28. In other work we suggested that the injected energy per baryon is only $u/\rho_0 c^2 \lesssim 20$ unless super-efficient neutrino mechanisms are invoked (McKinney 2005b; Ramirez-Ruiz & Socrates 2005). We also found that the energy released is larger than observed, suggesting an fairly inefficient generation of γ -rays. We find an energetically dominant, lower Γ jet component that may explain x-ray flashes. In our case the baryon-contamination problem is avoided by magnetic confinement of the jet against baryons from the disk. We find $\Gamma_\infty \sim 100 - 1000$, which is much larger than they found and this may avoid the compactness problem. The difference between their and our model is the presence of a magnetic field and a rotating black hole, which together drive the BZ-effect and a stronger evacuation of the polar jet region.

MHD simulations of jet propagation have been performed that correspond to weakly magnetized AGN jets, where $b^2/(2u) \lesssim 3.3$ and $b^2/\rho_0 < 0.2$ (Leismann et al. 2005). Our study suggests that this region may only be important for AGN Poynting-dominated jets at scales $r \gg 10^4 r_g$ once the jet becomes matter-dominated or may apply to the disk outflow.

Nonrelativistic MHD (Proga et al. 2003; Kato et al. 2004) and prior GRMHD simulations (Mizuno et al. 2004; Komissarov 2005) of jets showed a slow jet with $v \sim 0.2 - 0.3c$, insufficient to explain most jets from GRBs and AGN. Proga et al. (2003) suggested that their Poynting-dominated jet has $\Gamma_\infty \lesssim 10$, but they were unable to follow the relativistic jet using the nonrelativistic equations of motion. The previous GRMHD simulations created slow jets because of the “floor model” in the polar regions, the short time of integration, and the limited outer radius of the computational box.

De Villiers et al. (2005b) used a nonconservative numerical method to evolve a fully relativistic, black hole mass-invariant model, and showed a jet with hot blobs moving with $\Gamma \sim 50$. A primary result in agreement with the results here is that a patchy or pulsed “magnetic fireball” is produced. This suggests that the development of a “magnetic fireball” is not an artifact of the numerical implementation but is a result of shock heating. We also agree in finding that the core of the jet is hot and fast and is surrounded by a cold slow flow. One difference is that they say they seem to have found that the flow is cylindrically collimated by $r \gtrsim 300 r_g$, while we find nearly power-law collimation until $r \sim 10^3 r_g$ and an oscillatory conical asymptote beyond. They suggested that temporal variability is due to injection events near the black hole, while we suggest it is due to pinch (or perhaps kink) instabilities at $r \gtrsim 10^2 r_g$.

They found a larger value of Γ at smaller radius than we find. Indeed, one should wonder why their black hole mass-invariant model applies to only GRBs and not AGN or x-ray

binaries. This is a result of their *much* lower “floor” density of $\rho_0 \sim 10^{-12} \rho_{0,disk}$, which is far too low to be consistent with the self-consistent pair-loading (Popham et al. 1999) or neutron diffusion loading (Levinson & Eichler 2003) of the jet. Also, because they used a constant density floor, the jet region at large radius must be additionally loaded with an arbitrary amount of rest-mass. The typical “floor” model adds rest-mass into the comoving frame, but this artificially loads the jet with extra mass moving at high Γ . As applied to GRBs, we suggest that rather than the acceleration occurring within $r \lesssim 700r_g$ of their simulation, that acceleration occurs much farther away before the emitting region at $r \lesssim 10^9 r_g$. In their $\Gamma \sim 50$ knots the gas has $10^3 \lesssim u/\rho_0 c^2 \lesssim 10^6$. This implies that their actual terminal Lorentz factor is on the order of $10^5 \lesssim \Gamma_\infty \lesssim 10^7$, which would imply that the external shocks occur before internal shocks could occur.

6.5 Limitations

As has been pointed out by Komissarov (2005), *nonconservative* GRMHD schemes often overestimate or underestimate the amount of thermal energy produced. All numerical models suffer from some numerical error. Shock-conversion of magnetic energy to thermal energy is modelled by the *conservative* scheme in HARM in the perfect magnetic fluid approximation with total energy conserved exactly. However, our numerical model may still have overestimated the amount of magnetic dissipation in shocks, and a more accurate calculation may more slowly convert magnetic energy to thermal energy. However, we expect that toroidal field instabilities drive efficient magnetic dissipation as shown in the numerical results presented here. It is also encouraging that similar result are found in 3D nonrelativistic simulations (Ouyed et al. 2003) and maybe in the 2D relativistic simulations of De Villiers et al. (2005b) (they did not say why their jet generates hot blobs).

Confidence in the numerical results is obtained by code testing (Gammie et al. 2003a), comparisons with related analytical models (McKinney & Gammie 2004), and convergence testing the specific model being studied. For the fiducial model simulated in this paper, we used both higher and lower order spatial and temporal reconstructions and used a resolution smaller by a factor of two. The results described in the paper are independent of these numerical changes.

Unlike GRB neutrino-dominated disks, AGN and X-ray binaries may have accretion disks with a wide variety of H/R near the black hole, which could lead to a wide to narrow opening angle of the jet and disk wind. This broadness of the jet and wind may affect the classical viewing-angle-dependent unification models (Sauty et al. 2002). Only a self-consistent radiative GRMHD calculation can determine the disk thickness. The quantitative conclusions in this paper regarding the collimation angle assumed $H/R \sim 0.2$ near the black hole, while $H/R \sim 0.9$ (ADAF-like, Narayan & Yi 1995) is perhaps more appropriate for such systems. The sensitivity of these results to H/R is left for future work.

The simulations used a field geometry that was initially moderately organized, although there was no net field. As discussed in the introduction and in the floor model section, moderate changes in the initial geometry do not affect the results (McKinney & Gammie 2004). However, acc-

retion of a highly irregular (tangled) field would be quite different. An organized field may not develop around the black hole, and so disk material would mass-load the jet. In this case, the jet just becomes an extension of the disk wind (McKinney & Gammie 2004). However, the existence of a mostly uniform field threading the disk arises naturally during core-collapse supernovae and NS-BH collision debris disks. In AGN and stellar wind- capture x-ray binary systems, the accreted field may be uniform over long time scales (Narayan et al. 2003; Spruit & Uzdensky 2005). Roche-lobe overflow x-ray binaries, however, may accrete quite irregular field. The field geometry that arrives at the black hole, after travelling from the source of material (molecular torus, star(s), etc.) to the black hole horizon, should depend sensitively on the reconnection physics.

In order to evolve for a longer time than simulated in this paper, other physics must be included. For long-term evolution of a GRB model, one must include disk neutrino cooling, photodisintegration of nuclei, and a realistic equation of state. If one wishes to track nuclear species evolution, a nuclear burning reactions network is required. For the neutrino optically thick region of the disk, radiative transport should be included. The self-gravity of the star should be included to evolve the core-collapse. This includes a numerical relativity study of the collapse of a rotating magnetized massive star into a black hole (see review by Stergioulas 2003, §4.3). The jet should be followed through the entire star and beyond penetration of the stellar surface (Aloy et al. 2000; Zhang, Woosley, & MacFadyen 2003; Zhang W. et al. 2004).

As applied to all black hole accretion systems, some other limitations of the numerical models presented include the assumption of axisymmetry, ideal MHD, and a nonradiative gas.

The assumption of axisymmetry is not crucial for the basic structure of the inner jet region since our earlier results (McKinney & Gammie 2004) are in quantitative agreement with 3D results (De Villiers, Hawley, & Krolik 2003). The primary observed limitation of axisymmetry appears to be the decay of turbulence (Cowling 1934), which we attempted to avoid by requiring a resolution that gives quasi-steady turbulence for much of the simulation. Also, the jet at large distances has already formed by the time turbulence decays, and by that time the jet at large radius is not in causal contact with the disk.

When the toroidal field dominates the poloidal field, eventually $m = 1$ kink instabilities and higher modes may appear in 3D models (see, e.g., Nakamura et al. 2001; Ouyed et al. 2003; Nakamura & Meier 2004). Thus our 2D axisymmetric models may have underestimated the amount of oscillation in the flow and the conversion of Poynting flux to enthalpy flux. On the contrary, rotating Poynting-dominated jets may be marginally stable to kink instabilities (Tomimatsu et al. 2001), as suggested by our results.

The decay of turbulence due to the limitation of axisymmetry may also limit the efficiency of the Blandford-Znajek process. The magnetic arrested disk (MAD) model suggests that any accretion flow that accumulates a large amount of magnetic flux near the black hole eventually halts the accretion flow and builds a black hole magnetosphere (Igumenshchev et al. 2003; Narayan et al. 2003). This implies that the efficiency of extracting energy could be higher.

We have neglected high-energy particle and radiative processes in the numerical simulations. The floor model of the minimum allowed rest-mass density and internal energy density is ad hoc and chosen so that a fast jet emerges. Future work should include a model of pair creation and pair annihilation in order to simulate self-consistent mass-loading of the Poynting-dominated jet. A self-consistent model of the mass-loading can at least determine the density that should be present near the black hole around the poles. However, accurate determination of the Lorentz factor requires at least radiative transfer and Comptonization to model the radiative reaction within the jet that can slow or speed the jet.

For AGN and x-ray binaries, the radiatively inefficient disk approximation, which assumes electrons couple weakly to ions, may not hold. If the electrons and ions eventually couple near the black hole, then the disk might collapse into an unstable magnetically dominated accretion disk (MDAF) (Meier 2005). Like the MAD model, this might drastically alter the results here, although it is uncertain whether jets are actually produced under the conditions specified by the MDAF model.

The single-fluid, ideal MHD approximation breaks down under various conditions, such as during the quiescent output of AGN and x-ray black hole binaries, where a two-temperature plasma may form near the black hole as ions and electrons decouple (see, e.g., Narayan & Yi 1995). In some AGN and x-ray binary systems, the gas may no longer act like a fluid and nonthermal Fermi acceleration can produce a jet in a shear acceleration region between the disk and corona (Subramanian et al. 1999). Resistivity plays a role in current sheets where reconnection events may generate flares as on the sun, such as possibly observed in Sgr A (Genzel et al. 2003). Finally, radiative effects may introduce dynamically important instabilities in the accretion disk (e.g. Gammie 1998; Blaes & Socrates 2003).

6.6 Future Work

As applied to the collapsar model and other GRB models, future calculations will include a realistic equation of state; photodisintegration of nuclei; general relativistic ray-tracing neutrino transport (similar to, e.g., Broderick & Loeb 2005); neutrino cooling (similar to, e.g., Kohri et al. 2005); general relativistic accounting for the neutrino annihilation; neutrino Comptonization; simplified photon transport ; and photon Comptonization. The numerical calculations will also be performed in 3D.

As applied to AGN and x-ray binaries, future calculations will include general relativistic photon transport (similar to, e.g., Broderick & Loeb 2005); photon cooling; general relativistic accounting for the photon annihilation in the Poynting-dominated jet; photon Comptonization; and thermal and nonthermal synchrotron emission. The numerical calculations will also be performed in 3D.

The same type of calculation can be performed for systems harboring neutron stars, and this is a natural extension of recent force-free work (McKinney 2006a,b).

7 SUMMARY

A GRMHD code, HARM, was used to evolve black hole accretion disk models. Our work extends the results of previous GRMHD numerical models by studying the Poynting-dominated jet in more detail and studying the jet out to $r \sim 10^4 r_g$ till $t \sim 10^4 t_g$.

Basic results and conclusions include:

- (i) Poynting jet reaches $\Gamma \sim 10$ following nearly paraboloidal field lines and nearly $\Gamma \propto r^{1/2}$. Beyond $r \sim 10^3 r_g$, the jet has a conical outer angular part and a nearly paraboloidal core.
- (ii) Peak energy flux within the Poynting jet goes from $\theta_j \sim 60^\circ$ near the black hole to $\theta_j \sim 5^\circ$ at large distances.
- (iii) Energy structure of the Poynting jet is Gaussian with a half-width of $\theta_0 \approx 8^\circ$.
- (iv) Poynting jet has a core with flat energy flux within $\theta_j \approx 5^\circ$.
- (v) Extended slower Poynting jet component with $\theta_j \approx 27^\circ$.
- (vi) Poynting jet variability is dominated by toroidal field instabilities.
- (vii) Poynting jet is marginally kink stable.
- (viii) Poynting flux is shock-converted into enthalpy flux beyond Alfvén surface in an extended “shock zone.”
- (ix) Maximum terminal Lorentz factor is $\Gamma_\infty \lesssim 10^3$.
- (x) Poynting flux and enthalpy flux come into equipartition by $r \sim 10^3 r_g$.
- (xi) For radiation-dominated conditions, optically thick flows can tap thermal energy in adiabatic acceleration, while optically thin flows can lose thermal energy as radiation.
- (xii) Disk wind has collimated edge (near the Poynting jet) with $\Gamma \lesssim 1.5$.
- (xiii) Full disk wind is broad even near the black hole, and this may account for significant spatially-broad emission from near AGN cores, such as in M87.

ACKNOWLEDGMENTS

This research was supported by NASA-Astrophysics Theory Program grant NAG5-10780 and a Harvard CfA Institute for Theory and Computation fellowship. I thank Avery Broderick for an uncountable number of inspiring conversations. I also thank Charles Gammie, Brian Punsly, Amir Levinson, and Ramesh Narayan, with whom each I have had inspiring conversations. I thank Amir Levinson, Jonathan Granot, Maxim Lyutikov, Brian Punsly, Rob Fender, and Beskin Vasily for comments and discussions on the draft version of this paper. I thank Scott Noble for providing his highly efficient and accurate primitive variable solver. I thank Xiaoyue Guan for providing her implementation of parabolic interpolation.

REFERENCES

- Abramowicz, M., Jaroszinski, M., & Sikora, M. 1978, *A&A*, 63, 221
- Akiyama, S., Wheeler, J. C., Meier, D. L., & Lichtenstadt, I. 2003, *ApJ*, 584, 954

Aloy, M. A., Muller, E., Ibáñez, J. M., Marti, J. M., & MacFadyen, A. I. 2000, *ApJ*, 531, L119

Aloy, M.-A., Ibáñez, J.-M., Miralles, J.-A., & Urpin, V. 2002, *A&A*, 396, 693

Aloy, M. A., Janka, H.-T., Muller, E. 2005, *A&A*, 436, 273

Anile, A.M. 1989, *Relativistic Fluids and Magneto-fluids*, (New York: Cambridge Univ. Press)

Appl, S., & Camenzind, M. 1992, *A&A*, 256, 354

Appl, S. 1996, *A&A*, 314, 995

Balbus, S. A. & Hawley, J. F. 1991, *ApJ*, 376, 214

Begelman, M. C., Blandford, R. D., & Rees, M. J. 1984, *Reviews of Modern Physics*, 56, 255

Begelman, M. C., & Sikora, M. 1987, *ApJ*, 322, 650

Begelman, M. C., & Li, Z. 1994, *ApJ*, 426, 269

Begelman, M. C., Rees, M. J., & Sikora, M. 1994, *ApJ*, 429, L57

Begelman, M. C. 1998, *ApJ*, 493, 291

Berger, E., et al. 2003, *Nature*, 426, 154

Beskin, V. S. 1997, *Uspekhi Fizicheskikh Nauk*, 40, 659

Beskin, V. S., & Nokhrina, E. E. 2005, ArXiv Astrophysics e-prints, arXiv:astro-ph/0506333

Biretta, J. A., Sparks, W. B., & Macchetto, F. 1999, *ApJ*, 520, 621

Biretta, J. A., Junor, W., & Livio, M. 2002, *New Astronomy Review*, 46, 239

Bisnovatyi-Kogan, G. S., & Ruzmaikin, A. A. 1976, *Ap&SS*, 42, 401

Blaes, O., & Socrates, A. 2003, *ApJ*, 596, 509

Blandford, R. D. 1976, *MNRAS*, 176, 465

Blandford, R. D. & Znajek, R. L. 1977, *MNRAS*, 179, 433

Blandford, R. D. 2000, *Astronomy, physics and chemistry of H_3^+* , 358, 811

Blandford, R. D., & Levinson, A. 1995, *ApJ*, 441, 79

Bogovalov, S., & Tsinganos, K. 2005, *MNRAS*, 357, 918

Broderick, A. E., & Loeb, A. 2005, *MNRAS*, 363, 353

Celotti, A., & Fabian, A. C. 1993, *MNRAS*, 264, 228

Chiaberge, M., Celotti, A., Capetti, A., & Ghisellini, G. 2000, *A&A*, 358, 104

Clarke, D. A., Norman, M. L., & Burns, J. O. 1986, *ApJ*, 311, L63

Coburn, W. & Boggs, S. E. 2003, *Nature*, 423, 415

Colella, P., & Woodward, P., 1984, *JCP*, 54, 174

Cowling, T. G. 1934, *MNRAS*, 94, 768

Cui, W., Zhang, S. N., & Chen, W. 1998, *ApJ*, 492, L53

Daigne, F., & Drenkhahn, G. 2002, *A&A*, 381, 1066

De Villiers, J., Hawley, J. F., & Krolik, J. H. 2003, *ApJ*, 599, 1238

De Villiers, J., Hawley, J. F., Krolik, J. H., & Hirose, S. 2005, *ApJ*, 620, 878

De Villiers, J., Staff, J., & Ouyed, R. 2005, astro-ph/0502225

Di Matteo, T., Springel, V., & Hernquist, L. 2005, *Nature*, 433, 604

Drenkhahn, G. 2002, *A&A*, 387, 714

Drenkhahn, G. & Spruit, H. C. 2002, *A&A*, 391, 1141

Duncan, R. C. & Thompson, C. 1992, *ApJ*, 392, L9

Eichler, D. 1993, *ApJ*, 419, 111

Elvis, M. 2000, *ApJ*, 545, 63

Elvis, M., Risaliti, G., Nicastro, F., Miller, J. M., Fiore, F., & Puccetti, S. 2004, *ApJ*, 615, L25

Fabian, A. C., et al. 2002, *MNRAS*, 335, L1

Fender, R. 2003a, ArXiv Astrophysics e-prints, arXiv:astro-ph/0303339

Fender, R. P. 2003b, *MNRAS*, 340, 1353

Fender, R., & Belloni, T. 2004, *ARA&A*, 42, 317

Fendt, C., & Ouyed, R. 2004, *ApJ*, 608, 378

Fishbone, L.G., & Moncrief, V. 1976, *ApJ*, 207, 962

Frail, D. A., et al. 2001, *ApJ*, 562, L55

Gammie, C. F. 1998, *MNRAS*, 297, 929

Gammie, C. F., McKinney, J. C., & Gábor Tóth 2003, *ApJ*, 589, 444

Gammie, C. F., Shapiro, S. L., & McKinney, J. C. 2004, *ApJ*, 602, 312

Gammie, C. F. 2004, *ApJ*, 614, 309

Genzel, R., Schödel, R., Ott, T., Eckart, A., Alexander, T., Lacombe, F., Rouan, D., & Aschenbach, B. 2003, *Nature*, 425, 934

Gierliński, M., & Done, C. 2004, *MNRAS*, 347, 885

Ghirlanda, G., Celotti, A., & Ghisellini, G. 2003, *A&A*, 406, 879

Ghisellini, G., Padovani, P., Celotti, A., & Maraschi, L. 1993, *ApJ*, 407, 65

Ghisellini, G., & Madau, P. 1996, *MNRAS*, 280, 67

Ghisellini, G., Lazzati, D., Celotti, A., & Rees, M. J. 2000, *MNRAS*, 316, L45

Ghisellini, G., & Celotti, A. 2001, *MNRAS*, 327, 739

Ghisellini, G., Haardt, F., & Matt, G. 2004, *A&A*, 413, 535

Ghisellini, G., Tavecchio, F., & Chiaberge, M. 2005, *A&A*, 432, 401

Giannios, D., & Spruit, H. C. 2006, ArXiv Astrophysics e-prints, arXiv:astro-ph/0601172

Ghosh, P. & Abramowicz, M. A. 1997, *MNRAS*, 292, 887

Goldreich, P., & Julian, W. H. 1969, *ApJ*, 157, 869

Goodman, J. 1997, *New Astronomy*, 2, 449

Gracia, J., Tsinganos, K., & Bogovalov, S. V. 2005, *A&A*, 442, L7

Granot, J. & Königl, A. 2003, *ApJ*, 594, L83

Granot, J., & Taylor, G. B. 2005, *ApJ*, 625, 263

Greiner, J., Cuby, J. G., & McCaughrean, M. J. 2001, *Nature*, 414, 522

Guilbert, P. W., Fabian, A. C., & Rees, M. J. 1983, *MNRAS*, 205, 593

Heger, A., Woosley, S. E., & Spruit, H. C. 2005, *ApJ*, 626, 350

Hirose, S., Krolik, J. H., De Villiers, J., & Hawley, J. F. 2004, *ApJ*, 606, 1083

Hjorth, J., et al. 2003, *Nature*, 423, 847

Ho, L. C. 1999, *ApJ*, 516, 672

Igumenshchev, I. V., & Abramowicz, M. A. 1999, *MNRAS*, 303, 309

Igumenshchev, I. V., & Abramowicz, M. A. 2000, *ApJS*, 130, 463

Igumenshchev, I. V., Narayan, R., & Abramowicz, M. A. 2003, *ApJ*, 592, 1042

Jorstad, S. G., Marscher, A. P., Mattox, J. R., Wehrle, A. E., Bloom, S. D., & Yurchenko, A. V. 2001, *ApJS*, 134, 181

Junor, W., Biretta, J. A., & Livio, M. 1999, *Nature*, 401, 891

Kaiser, C. R., Gunn, K. F., Brocksopp, C., & Sokoloski, J. L. 2004, *ApJ*, 612, 332

Kalogera, V., Narayan, R., Spergel, D. N., & Taylor, J. H. 2001, *ApJ*, 556, 340

Kato, Y., Mineshige, S., & Shibata, K. 2004, *ApJ*, 605, 307

Kawabata, K. S., et al. 2003, *ApJ*, 593, L19

Kino, M., & Takahara, F. 2004, *MNRAS*, 349, 336

Khokhlov, A. M., Höflich, P. A., Oran, E. S., Wheeler, J. C., Wang, L., & Chtchelkanova, A. Y. 1999, *ApJ*, 524, L107

Kobayashi, S., Piran, T., & Sari, R. 1997, *ApJ*, 490, 92

Kohri, K., & Mineshige, S. 2002, *ApJ*, 577, 311

Kohri, K., Narayan, R., & Piran, T. 2005, *astro-ph/0502470*

Koide, S., Shibata, K., Kudoh, T., & Meier, D. L. 2002, *Science*, 295, 1688

Komissarov, S. S. 2004, *MNRAS*, 350, 1431

Komissarov, S. S. 2005, *MNRAS*, 359, 801

Konopelko, A., Mastichiadis, A., Kirk, J., de Jager, O. C., & Stecker, F. W. 2003, *ApJ*, 597, 851

Kouveliotou, C., et al. 1999, *ApJ*, 510, L115

Krawczynski, H., Coppi, P. S., & Aharonian, F. 2002, *MNRAS*, 336, 721

Krichbaum, T. P., et al. 2004, European VLBI Network on New Developments in VLBI Science and Technology, 15

Kulkarni, S. R., et al. 1998, *Nature*, 395, 663

Lamb, D. Q., Donaghy, T. Q., & Graziani, C. 2004, *New Astronomy Review*, 48, 459

Lazzati, D., Rossi, E., Ghisellini, G., & Rees, M. J. 2004, *MNRAS*, 347, L1

Lazzati, D., Begelman, M., Ghirlanda, G., Ghisellini, G., & Firmani, C. 2005, *astro-ph/0503630*

Leblanc, J. M. & Wilson, J. R. 1970, *ApJ*, 161, 541

Leismann, T., Antón, L., Aloy, M. A., Müller, E., Martí, J. M., Miralles, J. A., & Ibáñez, J. M. 2005, *A&A*, 436, 503

Levinson, A., & Blandford, R. 1996, *ApJ*, 456, L29

Levinson, A., & Eichler, D. 1993, *ApJ*, 418, 386

Levinson, A., & Eichler, D. 2003, *ApJ*, 594, L19

Levinson, A. 2005, *astro-ph/0502346*

Lewin, W. H. G., van Paradijs, J., & van den Heuvel, E. P. J. 1995, Cambridge Astrophysics Series, Cambridge, MA: Cambridge University Press, —c1995, edited by Lewin, Walter H.G.; Van Paradijs, Jan; Van den Heuvel, Edward P.J.,

Li, Z., Chiueh, T., & Begelman, M. C. 1992, *ApJ*, 394, 459

Li, Z.-Y. 1993, *ApJ*, 415, 118

Li, L. 2000, *ApJ*, 531, L111

Li, L. 2002, *ApJ*, 564, 108

Lind, K. R., Payne, D. G., Meier, D. L., & Blandford, R. D. 1989, *ApJ*, 344, 89

Livio, M., Ogilvie, G. I., & Pringle, J. E. 1999, *ApJ*, 512, 100

Lloyd-Ronning, N. M., Dai, X., & Zhang, B. 2004, *ApJ*, 601, 371

Lorimer, D. R. 2001, ArXiv Astrophysics e-prints, *arXiv:astro-ph/0104388*

Lovelace, R. V. E. 1976, *Nature*, 262, 649

Lyutikov, M., & Blackman, E. G. 2001, *MNRAS*, 321, 177

Lyutikov, M., & Blandford, R. 2003, ArXiv Astrophysics e-prints, *arXiv:astro-ph/0312347*

Lyutikov, M., Pariev, V. I., & Blandford, R. D. 2003, *ApJ*, 597, 998

MacFadyen, A. I. & Woosley, S. E. 1999, *ApJ*, 524, 262

Maraschi, L. & Tavecchio, F. 2003, *ApJ*, 593, 667

Martocchia, A., Matt, G., Karas, V., Belloni, T., & Feroci, M. 2002, *A&A*, 387, 215

McClintock, J. E., & Remillard, R. A. 2003, ArXiv Astrophysics e-prints, *arXiv:astro-ph/0306213*

McKinney, J. C., & Gammie, C. F. 2002, *ApJ*, 573, 728

McKinney, J. C. 2004, unpublished Ph.D. thesis, University of Illinois at Urbana-Champaign, <http://rainman.astro.uiuc.edu/~jon/research/thesis.pdf>

McKinney, J. C., & Gammie, C. F. 2004, *ApJ*, 611, 977

McKinney, J. C. 2005a, *ApJ*, 630, L5

McKinney, J. C. 2005b, *astro-ph/0506368*

McKinney, J. C. 2005c, *astro-ph/0506369*, v1

McKinney, J. C. 2006a, *MNRAS*, in press (*astro-ph/0601410*)

McKinney, J. C. 2006b, *MNRAS*, in press (*astro-ph/0601411*)

Meier, D. L. 2003, *New Astronomy Review*, 47, 667

Meier, D. L. 2005, *Ap&SS*, 300, 55

Merloni, A., Heinz, S., & di Matteo, T. 2003, *MNRAS*, 345, 1057

O. E. B. Messer, A. Mezzacappa, S. W. Bruenn, and M. W. Guidry, *Astrophys. J.* **507**, 353 (1998); S. Yamada, H-Th Janka, H. Suzuki, *Astron. Astrophys.* **344**, 533 (1999); A. Burrows, T. Young, P. Pinto, R. Eastman, T. A. Thompson, *Astrophys. J.* **539**, 865 (2000); M. Rampp, H-Th Janka, *Astrophys. J.* **539**, L33 (2000); M. Liebendoerfer, et al. *Phys. Rev. D* **63**, 104003-1 (2001).

Mészáros, P. 2002, *ARA&A*, 40, 137

Mészáros, P. & Rees, M. J. 1997, *ApJ*, 482, L29

Mirabel, I. F., Rodriguez, L. F., Cordier, B., Paul, J., & Lebrun, F. 1992, *Nature*, 358, 215

Miller-Jones, J. C. A., Fender, R. P., & Nakar, E. 2006, ArXiv Astrophysics e-prints, *arXiv:astro-ph/0601482*

Mirabel, I. F., & Rodriguez, L. F. 1994, *Nature*, 371, 46

Mirabel, I. F., & Rodríguez, L. F. 1999, *ARA&A*, 37, 409

Misner, C. W., Thorne, K. S., & Wheeler, J. A. 1973, *Gravitation*, San Francisco: W.H. Freeman and Co., 1973

Mizuno, Y., Yamada, S., Koide, S., & Shibata, K. 2004, *ApJ*, 615, 389

Mochkovitch, R., Hernanz, M., Isern, J., & Martin, X. 1993, *Nature*, 361, 236

Nakamura, M., Uchida, Y., & Hirose, S. 2001, *New Astronomy*, 6, 61

Nakamura, M., & Meier, D. L. 2004, *ApJ*, 617, 123

Narayan, R., Paczynski, B., & Piran, T. 1992, *ApJ*, 395, L83

Narayan, R. & Yi, I. 1995, *ApJ*, 452, 710

Narayan, R., Piran, T., & Kumar, P. 2001, *ApJ*, 557, 949

Narayan, R., Igumenshchev, I. V., & Abramowicz, M. A. 2003, *PASJ*, 55, L69

Noble, S.C. , Gammie, C.F., McKinney, J.C., Del Zanna, L.D., 2005, *ApJ*, accepted, *astro-ph/0512420*

Okamoto, I. 1999, *MNRAS*, 307, 253

Okamoto, I. 2000, *MNRAS*, 318, 250

Ouyed, R., Clarke, D. A., & Pudritz, R. E. 2003, *ApJ*, 582, 292

Paczynski, B. 1998, *ApJ*, 494, L45

Papaloizou, J. C. B. & Pringle, J. E. 1983, *MNRAS*, 202, 1181

Phinney, E.S. 1983, unpublished Ph.D. thesis, Cambridge University

Piran, T. 2005, *Reviews of Modern Physics*, 76, 1143

Popham, R., Woosley, S. E., & Fryer, C. 1999, *ApJ*, 518, 356

Proga, D., MacFadyen, A. I., Armitage, P. J., & Begelman, M. C. 2003, *ApJ*, 599, L5

Punsly, B., & Coroniti, F. V. 1990, *ApJ*, 354, 583

Punsly, B., & Coroniti, F. V. 1990, *ApJ*, 350, 518

Punsly, B. 2001, *Black hole gravitohydromagnetics*, Berlin: Springer, 2001, xii, 400 p., *Astronomy and astrophysics library*, ISBN 3540414665,

Ramirez-Ruiz, E., & Socrates, A. 2005, ArXiv Astrophysics e-prints, arXiv:astro-ph/0504257

Rees, M. J., Phinney, E. S., Begelman, M. C., & Blandford, R. D. 1982, *Nature*, 295, 17

Reynolds, C. S., di Matteo, T., Fabian, A. C., Hwang, U., & Canizares, C. R. 1996, *MNRAS*, 283, L111

Rosen, A., Hardee, P. E., Clarke, D. A., & Johnson, A. 1999, *ApJ*, 510, 136

Salpeter, E. E. 1964, *ApJ*, 140, 796

Sauty, C., Tsinganos, K., & Trussoni, E. 2002, LNP Vol. 589: *Relativistic Flows in Astrophysics*, 589, 41

Scheck, L., Aloy, M. A., Martí, J. M., Gómez, J. L., Müller, E. 2002, *MNRAS*, 331, 615

Shay, M. A., Drake, J. F., Rogers, B. N., & Denton, R. E. 2001, *J. Geophys. Res.*, 106, 3759

Shu, C.W., 1997, NASA/CR-97-206253, No.97-65

Sikora, M., Begelman, M. C., Coppi, P., & Proga, D. 2003, *ApJ*, submitted, astro-ph/0309504

Sikora, M., Begelman, M. C., Madejski, G. M., & Lasota, J. 2005, *ApJ*, 625, 72

Sikora, M., & Madejski, G. 2000, *ApJ*, 534, 109

Soderberg, A. M. & Ramirez-Ruiz, E. 2003, AIP Conf. Proc. 662: *Gamma-Ray Burst and Afterglow Astronomy 2001: A Workshop Celebrating the First Year of the HETE Mission*, 662, 172

Springel, V., Di Matteo, T., & Hernquist, L. 2004, ArXiv Astrophysics e-prints, arXiv:astro-ph/0411108

Spruit, H. C., & Taam, R. E. 1990, *A&A*, 229, 475

Spruit, H. C., Daigne, F., & Drenkhahn, G. 2001, *A&A*, 369, 694

Stergioulas, N. 2003, *Living Reviews in Relativity*, 6, 3

Stone, J. M., Pringle, J. E., & Begelman, M. C. 1999, *MNRAS*, 310, 1002

Subramanian, P., Becker, P. A., & Kazanas, D. 1999, *ApJ*, 523, 203

Symbalisty, E. M. D. 1984, *ApJ*, 285, 729

Stanek, K. Z., et al. 2003, *ApJ*, 591, L17

Taylor, G. B., Frail, D. A., Berger, E., & Kulkarni, S. R. 2004, *ApJ*, 609, L1

Taylor, G. B., Momjian, E., Pihlstrom, Y., Ghosh, T., & Salter, C. 2004, ArXiv Astrophysics e-prints, arXiv:astro-ph/0412483

Takahashi, M. , Nitta, S. , Tatematsu, Y. & Tomimatsu, A. 1990, *ApJ*, 363, 206

Tanaka, Y., et al. 1995, *Nature*, 375, 659

Thompson, C. 1994, *MNRAS*, 270, 480

Thompson, C., & Duncan, R. C. 1995, *MNRAS*, 275, 255

Thompson, C., & Duncan, R. C. 1996, *ApJ*, 473, 322

Thorsett, S. E., & Chakrabarty, D. 1999, *ApJ*, 512, 288

Tomimatsu, A. 1994, *PASJ*, 46, 123

Tomimatsu, A., Matsuoka, T., & Takahashi, M. 2001, *Phys. Rev. D*, 64, 123003

Tomimatsu, A., & Takahashi, M. 2003, *ApJ*, 592, 321

Tsinganos, K., & Bogoalov, S. 2005, AIP Conf. Proc. 745: *High Energy Gamma-Ray Astronomy*, 745, 148

Uemura, M., et al. 2003, *Nature*, 423, 843

Urry, C. M., & Padovani, P. 1995, *PASP*, 107, 803

Uzdensky, D. A. 2005, *ApJ*, 620, 889

Spruit, H. C., & Uzdensky, D. A. 2005, *ApJ*, 629, 960

Vlahakis, N. 2004, *Ap&SS*, 293, 67

Wang, L. & Wheeler, J. C. 1996, *ApJ*, 462, L27

Wang, L., Howell, D. A., Höflich, P., & Wheeler, J. C. 2001, *ApJ*, 550, 1030

Wang, L., et al. 2002, *ApJ*, 579, 671

Wang, L., Baade, D., Höflich, P., & Wheeler, J. C. 2003, *ApJ*, 592, 457

Wheeler, J. C., Yi, I., Höflich, P., & Wang, L. 2000, *ApJ*, 537, 810

Woosley, S. E. 1993, *ApJ*, 405, 273

Woosley, S. E., & Weaver, T. A. 1995, *ApJS*, 101, 181

Woosley, S. E. & Weaver, T. A. 1986, *ARA&A*, 24, 205

Woosley, S. E., Zhang, W., & Heger, A. 2003, *From Twilight to Highlight: The Physics of Supernovae*, 87

Zel'dovich Y. B. 1964, *Sov. Phys.-Dokl.*, 9, 195

Zhang, B., Dai, X., Lloyd-Ronning, N. M., & Mészáros, P. 2004, *ApJ*, 601, L119

Zhang, W., Woosley, S. E., & MacFadyen, A. I. 2003, *ApJ*, 586, 356

Zhang, W., Woosley, S. E., & Heger, A. 2004, *ApJ*, 608, 365

Zhang, W., & MacFadyen, A. I. 2005, astro-ph/0505481